

An adaptive enriched semi-Lagrangian finite element method for coupled flow-transport problems

Abdelouahed Ouardghi^a, Mofdi El-Amrani^{b,*}, Mohammed Seaid^{c,a}

^a*International Water Research Institute, University Mohammed VI Polytechnic, Benguerir, Morocco*

^b*Dpto. Matemáticas Aplicada, Ciencia e Ingeniería de Materiales y Tecnología Electrónica, Universidad Rey Juan Carlos, 28933 Móstoles-Madrid, Spain*

^c*Department of Engineering, University of Durham, South Road, DH1 3LE, UK*

Abstract

An adaptive enriched semi-Lagrangian finite element method is proposed for the numerical solution of coupled flow-transport problems on unstructured triangular meshes. The new method combines the semi-Lagrangian scheme to deal with the convection terms, the finite element discretization to manage irregular geometries, a direct conjugate-gradient algorithm to solve the generalized Stokes problem, and an adaptive L^2 -projection using quadrature rules to improve the efficiency and accuracy of the proposed method. In this study, the gradient of the temperature is used as an error indicator for the adaptation of enrichments by increasing the number of quadrature points where it is needed without refining the computational mesh. Unlike other adaptive finite element methods for coupled flow-transport problems, linear systems in the proposed enriched semi-Lagrangian finite element method preserve the same structure and size at each refinement in the adaptation procedure. In addition, due to the Lagrangian treatment of convection terms in this approach, the standard Courant-Friedrichs-Lewy condition is relaxed and the time truncation errors are reduced in the diffusion-reaction part. We assess the performance of the proposed method for a convection-diffusion problem with a known analytical solution and for the benchmark problem of thermal flow past a circular cylinder. We also solve a heat transport problem in the Mediterranean Sea to illustrate the ability of the method to resolve complex flow features in irregular geometries. Comparisons to the conventional semi-Lagrangian finite element method are also carried out in the current work. The obtained numerical results demonstrate the potential of the proposed method to capture the main flow features and support our expectations for an accurate and highly efficient enriched semi-Lagrangian finite element method for coupled flow-transport problems.

Keywords: Enriched finite elements; Semi-Lagrangian method; Transport problems; Incompressible Navier-Stokes equations; L^2 projection; Adaptive algorithm.

*Corresponding author

Email addresses: abdelouahed.ouardghi@um6p.ma (Abdelouahed Ouardghi), mofdi.elamrani@urjc.es (Mofdi El-Amrani), m.seaid@durham.ac.uk (Mohammed Seaid)

1. Introduction

Coupled flow-transport problems take place in many applications in science and engineering. This class of problems occur in various problems in nature and technology, for example in the simulation of heat exchangers [1], cooling of electronic equipments [2], fume cupboard ventilation [3, 4], geophysics such as climate predictions and oceanic flows [5]. The governing equations in these problems consist of coupling the incompressible Navier-Stokes equations with a convection-diffusion equation for the transport of temperature using the Boussinesq approximation, see for example [6, 7, 8, 9, 10, 11]. Developing robust numerical solvers for this set of problems is still challenging in the situation of convection-dominated flows for which convection terms are manifestly more important than the diffusion terms particularly if some nondimensional parameters such as the Reynolds number attend high values. There exist many numerical techniques in the literature to solve the coupled flow-transport equations. In case of convection-dominated flows, the conventional Eulerian finite element methods use up-stream weighting in their implementations to stabilize the discretization. For example, the most popular Eulerian finite element methods are the streamline up-wind Petrov-Galerkin methods [12, 13, 14], the Taylor-Galerkin methods [15, 16, 17] and the Galerkin/least-squares methods [18, 14, 19]. However, truncation errors generated by the time integration in these conventional Eulerian methods are dominant and require Courant-Friedrichs-Lewy (CFL) stability conditions which impose severe restrictions on the time steps used in the numerical computations. Eulerian-based methods for the incompressible Navier-Stokes equations have also been discussed in [20, 21, 22, 23, 24, 25, 26, 27, 28] among others. A dimension split method has been studied in [26] and a multi-stage Rosenbrock scheme has been applied to the incompressible Navier-Stokes equations in [28]. However, these methods fail to resolve flow structures at high Reynolds numbers. In [20], a multigrid adaptive unstructured finite element method has been proposed for the numerical solution of the incompressible Navier-Stokes equations. However, the adaptation process in this scheme requires assembling matrices at each time step which increases the computational cost. A compact mixed finite element method has been proposed in [21] to reduce the computing time for solving linear algebraic equations resulted from the discretization of incompressible Navier-Stokes equations but this study dealt with steady problems only. In [22, 23], a class of finite difference schemes have been implemented for space discretization of incompressible Navier-Stokes equations. However, the main drawback of these methods is that they are not able to resolve complex flow problems in irregular geometries. Numerical simulation of incompressible flows in parameterized pipes has been performed in [24]. Spectral collocation methods have also been studied in [27] for incompressible Navier-Stokes equations with variable density. To avoid the instability problems, authors in [25] proposed a high-order implicit preconditioned finite difference method to solve the incompressible flows using the pseudo-compressibility approach. However, restrictions related to the solution of nonlinear systems and Cartesian geometry decrease the efficiency of this method.

Semi-Lagrangian methods employ the modified method of characteristics and have been widely used in the literature to solve several problems in physical and engineering applications. Indeed, semi-Lagrangian finite element methods have been used for example in [29] for convection-diffusion problems, in [30] for incompressible Navier-Stokes

equations, in [31] for tidal flows, and in [10] for natural and mixed convection flows. The central idea in these semi-Lagrangian finite element methods lies in reformulating the governing equations using the Lagrangian coordinates defined by the characteristic curves associated with the considered problem. The time derivative and the advection term are combined in the total derivative as a directional derivative along the characteristics which can be viewed as a characteristic time-stepping algorithm. Therefore, the Lagrangian treatment in these methods greatly reduces the time truncation errors in the Eulerian methods, see for instance [11, 32]. In addition, semi-Lagrangian methods allow for higher time steps exceeding those permitted by the CFL stability condition in its Eulerian finite element counterpart for the convection-dominated flows. In [29, 30] a class of L^2 -projection semi-Lagrangian finite element methods has been proposed for convection-dominated problems and incompressible Navier-Stokes equations. Numerical comparisons between the conventional and L^2 -projection semi-Lagrangian finite element methods have also been reported in these references, and the L^2 -projection has been demonstrated higher accuracy and stronger stability than the conventional method. However, for practical applications in the convection-dominated coupled flow-transport problems, these methods may become computationally demanding due to the dense quadratures required for the L^2 -projection used for the evaluation of solutions at the departure points.

Reducing the computational cost in finite element methods has attracted many researchers in recent years. In this context, enriched finite element methods have emerged in the literature by incorporating enrichment functions into the approximation space. These methods, also known by partition of unity methods, were proposed in [33], who showed that the use of interpolation functions with the classical partition of unity property allows the approximation space in a numerical approximation to be enriched by the inclusion of other functions suitable for the problem at hand. Enriched finite element methods have been widely used to solve elastic waves and diffusion problems, see [34, 35] and further references are therein. Results presented in [34, 35] also demonstrate that enriched finite element methods offer a very large reduction in the number of degrees of freedom required to achieve a prescribed accuracy. However, the main drawback of these methods lies on the dense and ill conditioned systems to be solved at each time step in the simulations. To construct a locally conservative finite element method for solving the coupled flow-transport problems in porous media, authors in [36] enriched the approximation space of the continuous Galerkin method with element-wise constant functions. Local enrichments using piecewise constant functions have also been proposed in [37] for Galerkin finite element methods solving a problem in poromechanics. However, enrichment techniques presented in these references injected additional degrees of freedom to those already assembled in the Galerkin finite element discretization and therefore the resulting linear systems change the sizes at each enrichment step. Adaptive enriched Galerkin finite element methods have also been studied in [38] for miscible displacement problems for which piecewise constant functions have been used for both global and local enrichments. As a criterion for adaptation, authors employed the entropy residual as a posteriori error indicator but this procedure required primary solutions to evaluate the error indicator which may limit the computational performance of the method. Needless to mention that the extension of these enrichment procedures reported in [36, 37, 38] to the numerical solution of incompressible Navier-Stokes equations is not trivial.

The objective of the present work is to develop enriched semi-Lagrangian finite element methods for the numerical solution of incompressible Navier-Stokes/Boussinesq equations. A key advance over the partition of unity approaches is the use of multiple quadratures in the L^2 -projection, and this enables considerable efficiency gains to be made since the matrix in the linear system is fixed and reused throughout the time stepping procedure. One other objective is also to implement a multilevel adaptive algorithm for enrichments using the gradient of the temperature field as an error indicator. In contrast to the gradient-based h -adaptive finite element methods as those investigated in [39, 40, 41, 42, 43, 44, 45, 46, 38], linear systems in the proposed enriched semi-Lagrangian finite element method keep the same structure and size at each adaptation step. Indeed, an initial coarse mesh is needed for the gradient-based h -adaptive methods to compute a primary solution for estimation of the gradient. This yields error accumulations due to the coarse mesh used in the approximation and the computational cost becomes prohibitive due to multiple interpolations between adaptive meshes. The performance of the proposed method is assessed using several examples for coupled flow-transport problems including a heat transport problem in the Mediterranean Sea. For various parameters like the Reynolds numbers, multilevel enrichments and mesh refinements, results of the enriched semi-Lagrangian finite element method are compared with those computed using the conventional semi-Lagrangian finite element method and compared against each other. To the best of our knowledge, there are no such research studies on the numerical simulation of coupled flow-transport equations using enriched semi-Lagrangian finite element methods.

The present paper is organized as follows. The description of the model employed and the finite element discretization are presented in section 2. In section 3 we present the formulation of the enriched semi-Lagrangian finite element method. This section includes the implementation of the L^2 -projection procedure for the convection stage and the direct conjugate gradient algorithm to solve the generalized Stokes stage. Section 4 is devoted to the development of a new adaptive enriched semi-Lagrangian finite element method. In this section we also discuss the criteria used for adaptation of enrichments. In section 5, we examine the numerical performance of the proposed method using several examples of coupled flow-transport problems including a heat transport in the Mediterranean Sea. Our new approach is demonstrated to enjoy the expected efficiency as well as accuracy and stability. Concluding remarks are summarized in section 6.

2. Governing equations and finite element discretization

Let us consider a two-dimensional bounded domain Ω with a boundary Γ subjected to a thermal variation $(\Theta'_H - \Theta'_C)$, where Θ'_H and Θ'_C are respectively temperatures of the hot and cold boundary regions on Γ . The flow consists of a viscous Newtonian fluid under the Boussinesq assumption and convection-dominated. Hence, the Newtonian property of the fluid ensures a linear dependence between the shear stresses and the velocity gradients whereas the Boussinesq assumption guarantees the density differences are confined to the buoyancy forces without violating the incompressibility condition, see for instance [47, 48]. Thus, the governing equations are the unsteady Navier-Stokes/Boussinesq

equations given in a dimensional form as

$$\begin{aligned}\nabla \cdot \mathbf{u}' &= 0, \\ \rho_\infty \left(\frac{\partial \mathbf{u}'}{\partial t'} + \mathbf{u}' \cdot \nabla \mathbf{u}' \right) + \nabla p' - \mu \nabla^2 \mathbf{u}' &= \rho_\infty (1 - \beta' (\Theta' - \Theta'_\infty)) \mathbf{g}', \\ \rho_\infty c_p \left(\frac{\partial \Theta'}{\partial t'} + \mathbf{u}' \cdot \nabla \Theta' \right) - \alpha \nabla^2 \Theta' &= 0,\end{aligned}\tag{1}$$

where \mathbf{u}' is the velocity, p' the pressure, Θ' the temperature, ρ_∞ the reference density, μ the dynamic viscosity, c_p the specific heat at constant pressure, \mathbf{g}' the gravity force, β' the coefficient of thermal expansion, and α the thermal diffusivity coefficient. To rewrite the equations (1) in a dimensionless form we introduce the following variables

$$t = \frac{\alpha t'}{x_\infty^2}, \quad \mathbf{x} = \frac{\mathbf{x}'}{x_\infty}, \quad \mathbf{u} = \frac{x_\infty \mathbf{u}'}{\alpha}, \quad p = \frac{x_\infty^2 p'}{\rho_\infty \alpha^2}, \quad \Theta = \frac{\Theta' - \Theta_\infty}{\Theta_H - \Theta_C},$$

where the primed variables refer to dimensional quantities and the subscript ' ∞ ' indicates the reference quantities. We also define the kinematic viscosity ν , the Prandtl number Pr , the Reynolds number Re , the Grashof number Gr and Richardson number Ri as

$$\nu = \frac{\mu}{\rho_\infty}, \quad Pr = \frac{\nu}{\alpha}, \quad Re = \frac{u_\infty x_\infty}{\nu}, \quad Gr = \frac{g \beta' (\Theta_H - \Theta_C) x_\infty^3}{\nu^2}, \quad Ri = \frac{Gr}{Re^2}.\tag{2}$$

Hence, the dimensionless formulation of equations (1) is

$$\begin{aligned}\nabla \cdot \mathbf{u} &= 0, \\ \frac{\partial \mathbf{u}}{\partial t} + \mathbf{u} \cdot \nabla \mathbf{u} + \nabla p - \frac{1}{Re} \nabla^2 \mathbf{u} &= Ri \Theta \mathbf{e}, \\ \frac{\partial \Theta}{\partial t} + \mathbf{u} \cdot \nabla \Theta - \frac{1}{Pr Re} \nabla^2 \Theta &= 0,\end{aligned}\tag{3}$$

where $\mathbf{e} = (0, 1)^\top$ is the unit vector in the direction of gravity. Note that the equations (3) have to be solved in the spatial domain Ω for a time interval $]0, T]$ equipped with given boundary and initial conditions. In practice, these conditions dependent on the problem under study and their discussion is postponed for section 4 where numerical examples are discussed in details. Here, the parameters of interest, the Reynolds number Re is usually used to measure the relative importance of convection compared to diffusion in (3) whereas, the Richardson number Ri is used to quantify the effects of heat in the flow.

In the present study, the semi-Lagrangian finite element method can be interpreted as a fractional step technique for which the convective part in (3) is decoupled from the generalized Stokes/Boussinesq part during the time integration. Thus, at each time step, the temperature, velocity and pressure are updated by solving the convection equations

$$\begin{aligned}\frac{\partial \mathbf{u}}{\partial t} + \mathbf{u} \cdot \nabla \mathbf{u} &= \mathbf{0}, \\ \frac{\partial \Theta}{\partial t} + \mathbf{u} \cdot \nabla \Theta &= 0,\end{aligned}\tag{4}$$

then the Stokes/Boussinesq equations (3)

$$\begin{aligned}\nabla \cdot \mathbf{u} &= 0, \\ \frac{D\mathbf{u}}{Dt} + \nabla p - \frac{1}{Re} \nabla^2 \mathbf{u} &= Ri\Theta\mathbf{e}, \\ \frac{D\Theta}{Dt} - \frac{1}{PrRe} \nabla^2 \Theta &= 0,\end{aligned}\tag{5}$$

where $\frac{Dw}{Dt}$ is the material derivative of the generic physical variable w defined by

$$\frac{Dw}{Dt} = \frac{\partial w}{\partial t} + \mathbf{u} \cdot \nabla w.\tag{6}$$

To discretize the spatial domain $\bar{\Omega} = \Omega \cup \Gamma$, we generate a quasi-uniform partition $\Omega_h \subset \bar{\Omega}$ of triangular elements \mathcal{K}_l such that $\bar{\Omega} = \cup_{l=1}^{N_e} \mathcal{K}_l$, with N_e is the number of elements of Ω_h and h is a spatial discretization parameter. In this study, we consider the mixed Taylor-Hood finite elements P_2/P_1 for the conforming finite element spaces for the temperature, velocity and pressure *i.e.*, polynomials of second degree for the temperature and velocity solutions, and polynomials of first degree for the pressure solution. The associated finite element spaces are defined as

$$\begin{aligned}V_h &= \left\{ \Theta_h \in C^0(\bar{\Omega}) : \Theta_h|_{\mathcal{K}_j} \in P_2(\mathcal{K}_j), \quad \forall \mathcal{K}_j \in \Omega_h \right\}, \\ P_h &= \left\{ p_h \in C^0(\bar{\Omega}) : p_h|_{\mathcal{K}_j} \in P_1(\mathcal{K}_j), \quad \forall \mathcal{K}_j \in \Omega_h \right\},\end{aligned}$$

where $P_1(\mathcal{K}_j)$ and $P_2(\mathcal{K}_j)$ are respectively, the first-order and second-order polynomial spaces defined in the element \mathcal{K}_j . For the velocity field, the corresponding finite element space \mathbf{V}_h is defined by $\mathbf{V}_h = V_h \times V_h$. Note that for these finite elements, the discrete solutions of the temperature, velocity, and pressure satisfy the well-known inf-sup condition, see for instance [32]. For the time discretization, we divide $[0, T]$ into sub-intervals $[t_n, t_{n+1}]$ with uniform length $\Delta t = t_{n+1} - t_n$ for $n = 0, 1, \dots$. We also introduce the notation $w_h^n = w(\mathbf{x}_h, t_n)$ to denote the value of a generic solution w at the mesh point \mathbf{x}_h and time t_n . Thus, we formulate the finite element solutions $\Theta_h^n(\mathbf{x})$, $\mathbf{u}_h^n(\mathbf{x})$ and $p_h^n(\mathbf{x})$ as

$$\Theta_h^n(\mathbf{x}) = \sum_{j=1}^{M_v} \mathcal{T}_j^n \phi_j(\mathbf{x}), \quad \mathbf{u}_h^n(\mathbf{x}) = \sum_{j=1}^{M_v} \mathbf{U}_j^n \phi_j(\mathbf{x}), \quad p_h^n(\mathbf{x}) = \sum_{j=1}^{M_p} \mathcal{P}_j^n \psi_j(\mathbf{x}),\tag{7}$$

where M_v and M_p are respectively, the number of temperature/velocity and pressure mesh points in Ω_h . Here, the functions \mathcal{T}_j^n , $\mathbf{U}_j^n = (U_j^n, V_j^n)^\top$ and \mathcal{P}_j^n are respectively, the corresponding nodal values of $\Theta_h^n(\mathbf{x})$, $\mathbf{u}_h^n(\mathbf{x})$ and $p_h^n(\mathbf{x})$ defined as $\mathcal{T}_j^n = \Theta_h^n(\mathbf{x}_j)$, $\mathbf{U}_j^n = \mathbf{u}_h^n(\mathbf{x}_j)$ and $\mathcal{P}_j^n = p_h^n(\mathbf{y}_j)$ where $\{\mathbf{x}_j\}_{j=1}^{M_v}$ and $\{\mathbf{y}_j\}_{j=1}^{M_p}$ are respectively, the set of temperature, velocity and pressure mesh points in Ω_h so that $M_p < M_v$ and $\{\mathbf{y}_1, \dots, \mathbf{y}_{M_p}\} \subset \{\mathbf{x}_1, \dots, \mathbf{x}_{M_v}\}$. In (7), $\{\phi_j\}_{j=1}^{M_v}$ and $\{\psi_j\}_{j=1}^{M_p}$ are respectively, the set of global nodal basis functions of the temperature/velocity and the pressure characterized by the standard property $\phi_i(\mathbf{x}_j) = \delta_{ij}$ and $\psi_i(\mathbf{y}_j) = \delta_{ij}$ with δ denotes the Kronecker symbol.

3. Enriched semi-Lagrangian finite element method

In the conventional semi-Lagrangian finite element method, the characteristic curves $\mathcal{X}_{hj}^n = \mathcal{X}_h(t_n; \mathbf{x}_j, t_{n+1})$ associated with the convection problem (4) are calculated at any time t_n for each mesh point \mathbf{x}_j , $j = 1, \dots, M_v$ by solving

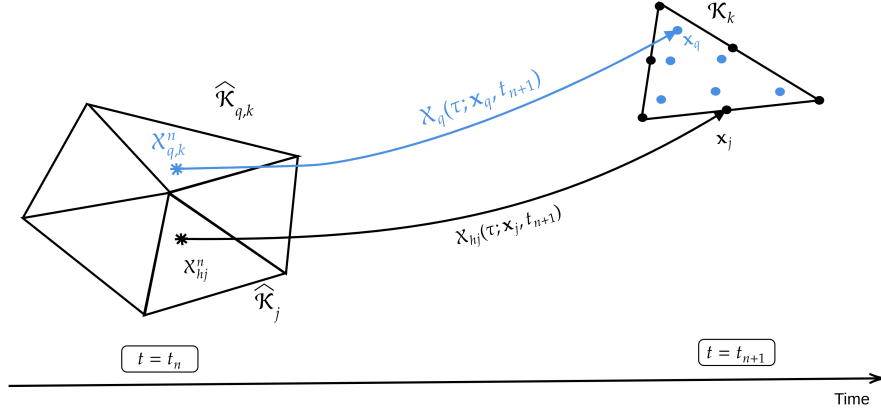


Figure 1: Illustration of departure points in the conventional method (points in black) and in the L^2 -projection method (points in blue). Here, departure points are computed for nodal points in the conventional method and for each Gauss point in the L^2 -projection method.

the initial-value problem

$$\begin{aligned} \frac{d\mathcal{X}_h(t; \mathbf{x}_j, t_{n+1})}{dt} &= \mathbf{u}_h(t, \mathcal{X}_h(t; \mathbf{x}_j, t_{n+1})), \quad \forall t \in [t_n, t_{n+1}], \\ \mathcal{X}_h(t_{n+1}; \mathbf{x}_j, t_{n+1}) &= \mathbf{x}_j, \quad j = 1, \dots, M_V. \end{aligned} \quad (8)$$

Notice that $\mathcal{X}_h(t; \mathbf{x}_j, t_{n+1}) := (X_h(t; \mathbf{x}_j, t_{n+1}), Y_h(t; \mathbf{x}_j, t_{n+1}))^\top$ is the departure point defined at time t of a fluid particle that will arrive in the mesh point $\mathbf{x}_j = (x_j, y_j)^\top$ at time t_{n+1} as illustrated in Figure 1. To solve the backward differential equations (8), we use the second-order extrapolation method based on the mid-point rule studied in [49, 29, 31] among others. In general, the calculated departure points \mathcal{X}_{hj}^n do not coincide with a mesh point in Ω_h and therefore a search-locate algorithm is required to identify the host element $\widehat{\mathcal{K}}_j$ where these points belong. In the current work, we use the search-locate algorithm proposed in [50] for triangular elements in unstructured grids.

Let us assume that the pairs $(\mathcal{X}_{hj}^n, \widehat{\mathcal{K}}_j)$ are known for all $j = 1, \dots, M_V$, we then compute the nodal solutions $\widehat{\mathcal{T}}_j^n$ and $\widehat{\mathbf{u}}_j^n = (\widehat{U}_j^n, \widehat{V}_j^n)^\top$ as

$$\widehat{\mathcal{T}}_j^n := \Theta_h^n(\mathcal{X}_{hj}^n) = \sum_{i=1}^N \Theta_h^n(\widehat{\mathbf{x}}_i) \varphi_i(\mathcal{X}_{hj}^n), \quad \widehat{\mathbf{u}}_j^n := \mathbf{u}_h^n(\mathcal{X}_{hj}^n) = \sum_{i=1}^N \mathbf{u}_h^n(\widehat{\mathbf{x}}_i) \varphi_i(\mathcal{X}_{hj}^n), \quad (9)$$

where $\{\varphi_i\}_{i=1}^N$ are the local basis functions associated with the element $\widehat{\mathcal{K}}_j$, with N is the number of nodes which define the temperature/velocity mesh grid, and $\{\widehat{\mathbf{x}}_i\}_{i=1}^N$ are the vertices of the host element $\widehat{\mathcal{K}}_j$. Recall that in the conventional semi-Lagrangian finite element method, the global solutions $\Theta_h^{n+1}(\mathbf{x})$ and $\mathbf{u}_h^{n+1}(\mathbf{x})$ of the convection equations (4) are computed by

$$\Theta_h^{n+1}(\mathbf{x}) = \Theta_h^n(\mathcal{X}_h^n) = \widehat{\Theta}_h^n(\mathbf{x}), \quad \mathbf{u}_h^{n+1}(\mathbf{x}) = \mathbf{u}_h^n(\mathcal{X}_h^n) = \widehat{\mathbf{u}}_h^n(\mathbf{x}), \quad (10)$$

where

$$\widehat{\Theta}_h^n(\mathbf{x}) = \sum_{j=1}^{M_v} \widehat{\mathcal{T}}_j^n \phi_j(\mathbf{x}), \quad \widehat{\mathbf{u}}_h^n(\mathbf{x}) = \sum_{j=1}^{M_v} \widehat{\mathbf{U}}_j^n \phi_j(\mathbf{x}). \quad (11)$$

It is well established that the accuracy of the conventional semi-Lagrangian finite element approximations (10)-(11) highly depend on the density of meshes used in the simulation. Furthermore, it has been shown in [29, 30] that the conventional semi-Lagrangian finite element method fails to resolve steep gradients for convection-dominated problems unless very fine meshes are employed in the simulations. In the current study, to overcome this drawback and to improve the accuracy of the semi-Lagrangian finite element method, we propose a class of local enrichments using the L^2 -projection.

3.1. L^2 -projection for local enrichments

A family of L^2 -projection methods has been investigated in [30, 29] for the semi-Lagrangian finite element approximation of convection-dominated flow problems. In this section we formulate the L^2 -projection as a local enrichment technique for the semi-Lagrangian finite element solutions (10)-(11). Thus, multiplying both sides of equation (10) by the finite element basis functions ϕ_i and integrating over Ω yields

$$\int_{\Omega} \Theta_h^{n+1}(\mathbf{x}) \phi_i(\mathbf{x}) dx = \int_{\Omega} \Theta_h^n(\mathcal{X}_h^n) \phi_i(\mathbf{x}) dx, \quad \int_{\Omega} \mathbf{u}_h^{n+1}(\mathbf{x}) \phi_i(\mathbf{x}) dx = \int_{\Omega} \mathbf{u}_h^n(\mathcal{X}_h^n) \phi_i(\mathbf{x}) dx, \quad i = 1, \dots, M_v. \quad (12)$$

Thus, the finite element solutions $\Theta_h^{n+1}(\mathbf{x})$ and $\mathbf{u}_h^{n+1}(\mathbf{x})$ can be formulated as

$$\Theta_h^{n+1}(\mathbf{x}) = \sum_{j=1}^{M_v} \mathcal{T}_j^{n+1} \phi_j(\mathbf{x}), \quad \mathbf{u}_h^{n+1}(\mathbf{x}) = \sum_{j=1}^{M_v} \mathbf{U}_j^{n+1} \phi_j(\mathbf{x}), \quad (13)$$

where \mathcal{T}_j^{n+1} and \mathbf{U}_j^{n+1} are the nodal coefficients of the solutions to be evaluated. Replacing the solution (13) in the left-hand side of equation (12) we obtain

$$\int_{\Omega} \Theta_h^{n+1}(\mathbf{x}) \phi_i(\mathbf{x}) dx = \sum_{j=1}^{M_v} \mathcal{T}_j^{n+1} \int_{\Omega} \phi_j(\mathbf{x}) \phi_i(\mathbf{x}) dx := \sum_{j=1}^{M_v} m_{ij} \mathcal{T}_j^{n+1}, \quad i = 1, \dots, M_v, \quad (14)$$

and

$$\int_{\Omega} \mathbf{u}_h^{n+1}(\mathbf{x}) \phi_i(\mathbf{x}) dx = \sum_{j=1}^{M_v} \mathbf{U}_j^{n+1} \int_{\Omega} \phi_j(\mathbf{x}) \phi_i(\mathbf{x}) dx := \sum_{j=1}^{M_v} m_{ij} \mathbf{U}_j^{n+1}, \quad i = 1, \dots, M_v, \quad (15)$$

with $m_{ij} = \int_{\Omega} \phi_j(\mathbf{x}) \phi_i(\mathbf{x}) dx$ are entries of the elemental mass matrix. To calculate the integrals in the right-hand side of equation (12) we use a quadrature rule as

$$\begin{aligned} \int_{\Omega} \Theta_h^n(\mathcal{X}_h^n) \phi_i(\mathbf{x}) dx &= \sum_{l=1}^{N_e} \int_{\mathcal{K}_l} \Theta_h^n(\mathcal{X}_h^n) \phi_i(\mathbf{x}) dx, \\ &\approx \sum_{l=1}^{N_e} \sum_{q=1}^{N_{l,Q}} \omega_{q,l} \Theta_h^n(\mathcal{X}_{q,l}^n) \phi_i(\mathbf{x}_{q,l}), \\ &\approx \sum_{l=1}^{N_e} \sum_{q=1}^{N_{l,Q}} \omega_{q,l} \widehat{\mathcal{T}}_{q,l}^n \phi_i(\mathbf{x}_{q,l}) := r_i^n, \quad i = 1, \dots, M_v, \end{aligned} \quad (16)$$

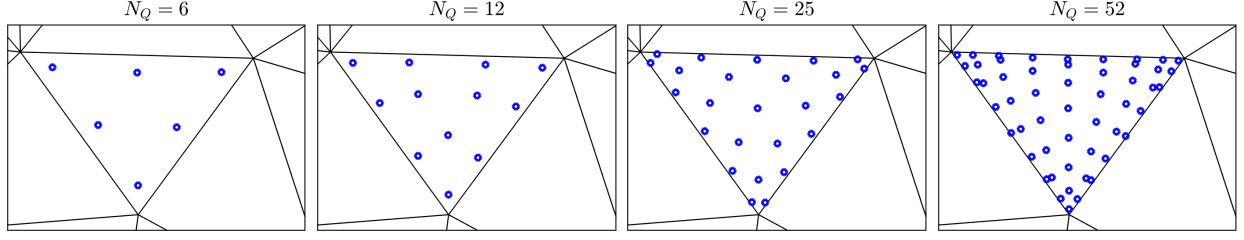


Figure 2: Distributions of quadrature points in a finite element used in the L^2 -projection method for global and local enrichments.

where $\mathbf{x}_{q,l} = (x_{q,l}, y_{q,l})^\top$ are the quadrature points associated with the finite element \mathcal{K}_l with weights $\omega_{q,l}$ and $N_{l,Q}$ is the total number of quadrature points in \mathcal{K}_l . Here, $\mathcal{X}_{q,l}^n$ is the departure point that will reach the quadrature point $\mathbf{x}_{q,l}$ at time t_{n+1} and $\widehat{\mathcal{T}}_{q,l}^n = \Theta_h^n(\mathcal{X}_{q,l}^n)$ is the solution evaluated at the departure point $\mathcal{X}_{q,l}^n$. Similarly,

$$\begin{aligned}
\int_{\Omega} \mathbf{u}_h^n(\mathcal{X}_h^n) \phi_i(\mathbf{x}) \, d\mathbf{x} &= \sum_{l=1}^{N_e} \int_{\mathcal{K}_l} \mathbf{u}_h^n(\mathcal{X}_h^n) \phi_i(\mathbf{x}) \, d\mathbf{x}, \\
&\approx \sum_{l=1}^{N_e} \sum_{q=1}^{N_{l,Q}} \omega_{q,l} \mathbf{u}_h^n(\mathcal{X}_{q,l}^n) \phi_i(\mathbf{x}_{q,l}), \\
&\approx \sum_{l=1}^{N_e} \sum_{q=1}^{N_{l,Q}} \omega_{q,l} \widehat{\mathbf{u}}_{q,l}^n \phi_i(\mathbf{x}_{q,l}) := \mathbf{z}_i^n, \quad i = 1, \dots, M_v,
\end{aligned} \tag{17}$$

where $\widehat{\mathbf{u}}_{q,l}^n = \mathbf{u}_h^n(\mathcal{X}_{q,l}^n)$ is the velocity solution evaluated at the departure point $\mathcal{X}_{q,l}^n$. Using the approximations (14)-(17), the equation (12) can be formulated as

$$\sum_{j=1}^{M_v} m_{ij} \mathcal{T}_j^{n+1} = \mathbf{r}_i^n, \quad \sum_{j=1}^{M_v} m_{ij} \mathbf{u}_j^{n+1} = \mathbf{z}_i^n, \quad i = 1, \dots, M_v. \tag{18}$$

Using the quadrature rule to approximate the integral, we obtain

$$m_{ij} = \int_{\Omega} \phi_j(\mathbf{x}) \phi_i(\mathbf{x}) \, d\mathbf{x} \approx \sum_{l=1}^{N_e} \sum_{q=1}^{N_{l,Q}} \omega_{q,l} \phi_j(\mathbf{x}_{q,l}) \phi_i(\mathbf{x}_{q,l}). \tag{19}$$

To compute the solutions $\widehat{\mathcal{T}}_{q,l}^n$ and $\widehat{\mathbf{u}}_{q,l}^n$ in (16) and (17) respectively, we assume that for each quadrature point $\mathbf{x}_{q,l}$ ($q = 1, \dots, N_{l,Q}$), the pair $(\mathcal{X}_{q,l}^n, \widehat{\mathcal{K}}_{q,l})$ is known, with $\widehat{\mathcal{K}}_{q,l}$ is the host element where the departure point $\mathcal{X}_{q,l}^n$ is located. Hence, as in the approximation (9), we compute the solutions $\widehat{\mathcal{T}}_{q,l}^n$ and $\widehat{\mathbf{u}}_{q,l}^n$ as

$$\widehat{\mathcal{T}}_{q,l}^n = \sum_{i=1}^N \Theta_h^n(\widehat{\mathbf{x}}_i) \varphi_i(\mathcal{X}_{q,l}^n), \quad \widehat{\mathbf{u}}_{q,l}^n = \sum_{i=1}^N \mathbf{u}_h^n(\widehat{\mathbf{x}}_i) \varphi_i(\mathcal{X}_{q,l}^n), \tag{20}$$

with $\{\widehat{\mathbf{x}}_i\}_{i=1}^N$ are the nodes of the host element $\widehat{\mathcal{K}}_{q,l}$ and $\{\varphi_i\}_{i=1}^N$ are their associated local basis functions. The equations (18) can also be assembled in a global matrix-vector form as

$$[\mathbf{M}] \{\mathcal{T}^{n+1}\} = \{\mathbf{r}^n\}, \quad [\mathbf{M}] \{\mathbf{u}^{n+1}\} = \{\mathbf{z}^n\}, \tag{21}$$

Algorithm 1 Enriched semi-Lagrangian finite element algorithm.

1: Assemble the finite element mass matrix $[\mathbf{M}]$ using (19).

Assuming that the nodal solutions \mathcal{T}^n and \mathbf{U}^n at the current time t_n is known.

2: **for** each element \mathcal{K}_i in the computational mesh **do**

3: Generate the quadrature $(\mathbf{x}_{q,l}, \omega_{q,l})$, $q = 1, \dots, N_{l,Q}$ using the Dunavant rule.

4: For each quadrature point $\mathbf{x}_{q,l}$ in the element \mathcal{K}_i , compute the departure point $\mathcal{X}_{q,l}^n$ by solving the initial-value problem (8).

5: Search-locate the mesh element $\widehat{\mathcal{K}}_{q,l}$ where the departure point $\mathcal{X}_{q,l}^n$ resides.

6: Evaluate the solution values $\widehat{\mathcal{T}}_{q,l}^n$ and $\widehat{\mathbf{U}}_{q,l}^n$ using the approximations

$$\widehat{\mathcal{T}}_{q,l}^n = \sum_{i=1}^N \Theta_h^n(\widehat{\mathbf{x}}_i) \varphi_i(\mathcal{X}_{q,l}^n), \quad \widehat{\mathbf{U}}_{q,l}^n = \sum_{i=1}^N \mathbf{u}_h^n(\widehat{\mathbf{x}}_i) \varphi_i(\mathcal{X}_{q,l}^n).$$

7: Compute the right-hand side elements r_i^n and \mathbf{z}_i^n using (16) and (??), then assemble the right hand sides in the vectors $\{\mathbf{r}^n\}$ and $\{\mathbf{z}^n\}$.

8: **end for**

9: Solve the linear systems

$$[\mathbf{M}] \{\mathcal{T}^{n+1}\} = \{\mathbf{r}^n\}, \quad [\mathbf{M}] \{\mathbf{U}^{n+1}\} = \{\mathbf{z}^n\},$$

to obtain the solutions \mathcal{T}^{n+1} and \mathbf{U}^{n+1} .

10: Calculate the solutions Θ_h^{n+1} and \mathbf{u}_h^{n+1} at time t_{n+1} according to the equation (13).

where $[\mathbf{M}]$ is the $M_v \times M_v$ -valued mass matrix with entries m_{ij} , \mathcal{T}^{n+1} and \mathbf{U}^{n+1} are the M_v -valued vectors of the unknown nodal solutions with entries \mathcal{T}_j^{n+1} and \mathbf{U}_j^{n+1} , respectively. In (21), \mathbf{r}^n and \mathbf{z}^n are the M_v -valued of the known right-hand sides with entries r_i^n and \mathbf{z}_i^n , respectively. It is worth mentioning that equation (18) can be viewed as an enrichment technique with the quadrature rules are used for enrichment functions. In (19), the number of quadrature points $N_{l,Q}$, their abscissa $\mathbf{x}_{q,l}$ and weights $\omega_{q,l}$ can be adjusted either globally in all elements of the mesh or locally at each element in the computational domain. In the present work, we considered the well-established Dunavant quadrature rules [51] for which the associated abscissa $\mathbf{x}_{q,l}$ and weights $\omega_{q,k}$ can be found therein. For an illustration, Figure 2 depicts the distribution of these quadrature points with $N_{l,Q} = 6, 12, 25$ and 52 . It should be noted that other quadrature rules can also be easily implemented in our method without major conceptual modifications.

In summary, Algorithm 1 describes the steps required in the enriched semi-Lagrangian finite element method for solving the convection problem (3). It should be stressed that no linear systems of algebraic equations need to be solved for the conventional semi-Lagrangian finite element method and the numerical solution is directly obtained by interpolation using the basis functions of the host element $\widehat{\mathcal{K}}_i$ where the departure points \mathcal{X}_i^n , $i = 1, \dots, M_v$ are localized. Unlike this conventional method, the proposed enriched semi-Lagrangian finite element method computes the departure points $\mathcal{X}_{q,l}^n$ for all quadrature points belonging to each element \mathcal{K}_i in the computational mesh and it also

requires solution of a linear system in order to update the numerical solution at each time step.

3.2. Solution of the generalized Stokes problem

In the current work, we implement a direct-type algorithm to solve the generalized Stokes problem (3), see for instance [52, 32, 53] for similar techniques. The main advantage of this algorithm lies on the fact that neither projection techniques nor special corrections for the pressure are needed in its implementation. To complete the formulation of the enriched semi-Lagrangian finite element method for the coupled flow-transport problem (1), we use a conjugate gradient method to directly solve the equations (3) for the temperature, velocity and pressure at each time step. The time integration is achieved using the second-order implicit scheme of Gear type also known in the literature by backward differentiation formula (BDF2). Hence, given a tolerance ε and using superscripts in parenthesis to refer to iteration numbers, the procedure to advance the solution of (3) from a time t_n to the next time t_{n+1} can be carried out in the following steps:

1. Solve for $\Theta_h^{n+1} \in V_h$ such that for all $v_h \in V_h$

$$\frac{3}{2\Delta t} \int_{\Omega} \Theta_h^{n+1} v_h \, dx + \frac{1}{PrRe} \int_{\Omega} \nabla \Theta_h^{n+1} \cdot \nabla v_h \, dx = \frac{1}{2\Delta t} \int_{\Omega} (4\widehat{\Theta}_h^n - \widehat{\Theta}_h^{n-1}) v_h \, dx \quad (22)$$

2. Given $p_h^{(0)} = p_h^n$, solve for $\mathbf{u}_h^{(0)} \in \mathbf{V}_h$ such that for all $\mathbf{v}_h \in \mathbf{V}_h$

$$\begin{aligned} \frac{3}{2\Delta t} \int_{\Omega} \mathbf{u}_h^{(0)} v_h \, dx + \frac{1}{Re} \int_{\Omega} \nabla \mathbf{u}_h^{(0)} \cdot \nabla v_h \, dx &= \int_{\Omega} p_h^{(0)} \nabla \cdot \mathbf{v}_h \, dx + Ri \int_{\Omega} \Theta_h^{n+1} v_h \cdot \mathbf{e} \, dx + \\ &\frac{1}{2\Delta t} \int_{\Omega} (4\widetilde{\mathbf{u}}_h^n - \widetilde{\mathbf{u}}_h^{n-1}) v_h \, dx. \end{aligned} \quad (23)$$

Then, compute

$$q_h^{(0)} = \nabla \cdot \mathbf{u}_h^{(0)}.$$

3. Solve for $\psi_h^{(0)} \in P_h$ such that for all $\psi_h \in P_h$

$$\int_{\Omega} \nabla \psi_h^{(0)} \cdot \nabla \psi_h \, dx = \int_{\Omega} q_h^{(0)} \psi_h \, dx, \quad (24)$$

and set

$$\zeta_h^{(0)} = \frac{3}{2\Delta t} \psi_h^{(0)} + \frac{1}{Re} q_h^{(0)}, \quad \xi_h^{(0)} = \zeta_h^{(0)}.$$

4. For $k = 1, 2, \dots$, assume that $p_h^{(k)}, \mathbf{u}_h^{(k)}, q_h^{(k)}, \zeta_h^{(k)}, \xi_h^{(k)}$ are known, we compute $p_h^{(k+1)}, \mathbf{u}_h^{(k+1)}, q_h^{(k+1)}, \zeta_h^{(k+1)}, \xi_h^{(k+1)}$ as follows:

- (a) Solve for $\bar{\mathbf{u}}_h \in \mathbf{V}_h$ such that for all $\mathbf{v}_h \in \mathbf{V}_h$

$$\frac{3}{2\Delta t} \int_{\Omega} \bar{\mathbf{u}}_h^{(k)} v_h \, dx + \frac{1}{Re} \int_{\Omega} \nabla \bar{\mathbf{u}}_h^{(k)} \cdot \nabla v_h \, dx = \int_{\Omega} \xi_h^{(k)} \nabla \cdot \mathbf{v}_h \, dx, \quad (25)$$

and set

$$\bar{q}_h^{(k)} = \nabla \cdot \bar{\mathbf{u}}_h^{(k)}.$$

(b) Compute

$$\eta_k = \frac{\int q_h^{(k)} \zeta_h^{(k)} dx}{\int \bar{q}_h^{(k)} \xi_h^{(k)} dx}.$$

(c) Set

$$p_h^{(k+1)} = p_h^{(k)} - \eta_k \zeta_h^{(k)}, \quad \mathbf{u}_h^{(k+1)} = \mathbf{u}_h^{(k)} - \eta_k \bar{\mathbf{u}}_h^{(k)}, \quad q_h^{(k+1)} = q_h^{(k)} - \eta_k \bar{q}_h^{(k)}.$$

(d) Solve for $\bar{\psi}_h^{(k)} \in P_h$ such that for all $\psi_h \in P_h$

$$\int \nabla \bar{\psi}_h^{(k)} \cdot \nabla \psi_h dx = \int \bar{q}_h^{(k)} \psi_h dx, \quad (26)$$

and set

$$\zeta_h^{(k+1)} = \zeta_h^{(k)} - \eta_k \left(\frac{3}{2\Delta t} \bar{\psi}_h^{(k)} + \frac{1}{Re} q_h^{(k)} \right).$$

i. If $\frac{\int q_h^{(k+1)} \zeta_h^{(k+1)} dx}{\int q_h^{(0)} \zeta_h^{(0)} dx} \leq \varepsilon$, then

$$p_h^{n+1} = p_h^{(k+1)}, \quad \mathbf{u}_h^{n+1} = \mathbf{u}_h^{(k+1)},$$

stop.

ii. Else, compute

$$\chi_k = \frac{\int q_h^{(k+1)} \zeta_h^{(k+1)} dx}{\int q_h^{(k)} \zeta_h^{(k)} dx}, \quad \xi_h^{(k+1)} = \zeta_h^{(k+1)} + \chi_k \xi_h^{(k)},$$

change $k \leftarrow k + 1$, return to step (a) and repeat.

iii. End if

It should be stressed that in (22)-(23), the solutions $\widehat{\Theta}^{n-1}$, $\widehat{\Theta}^n$, $\bar{\mathbf{u}}_h^n$ and $\bar{\mathbf{u}}_h^{n-1}$ are required to advance the solutions Θ^{n+1} and $\mathbf{u}_h^{(k)}$ in time. Here, at time $t = 0$ only one initial condition is provided and to obtain the second condition we use the implicit Euler scheme. Notice that the iterative process in the direct-type algorithm involves solutions of uncoupled elliptic problems such that their finite element discretization yields well-conditioned linear systems of algebraic equations for which very efficient solvers can be used. Taking advantage of these properties the linear systems in our enriched semi-Lagrangian algorithm can be solved by the conjugate gradient solver using an incomplete Cholesky factorization. It is also worth remarking that the finite element discretization of the equations (22)-(26) is straightforward and is omitted here.

4. Multilevel adaptive enrichments

In many applications in coupled flow-transport problems, the Reynolds number reaches high values for which steep gradients, localized eddies and boundary shear layers occur in their numerical solutions. In regions where the

Algorithm 2 Algorithm for the adaptive enriched semi-Lagrangian finite element method.

Require: $\varepsilon_m, m = 0, 1, 2, 3$.

```

1: while  $t_{n+1} \leq T$  do
2:   for each mesh triangle  $\mathcal{K}_l$  do
3:     Evaluate the error indicator  $\eta_{\mathcal{K}_l}^{n+1}$  using the equation (27).
4:     for  $m = 0, 1, 2, 3$  do
5:       if  $\varepsilon_m \leq \eta_{\mathcal{K}_l}^{n+1} \leq \varepsilon_{m+1}$  then
6:          $N_{l,Q} = N_{Q_m}$ 
7:       end if
8:     end for
9:   end for
10:  Generate the quadrature rule  $(\mathbf{x}_{q,l}, \omega_{q,l}), q = 1, \dots, N_{l,Q}$ .
11:  Compute the  $L^2$ -projection mass matrix  $[\mathbf{M}]$  using the equation (19).
12:  for each element  $\mathcal{K}_l$  do
13:    for each quadrature point  $\mathbf{x}_{q,l}, q = 1, \dots, N_{l,Q}$  do
14:      Compute the departure point  $\mathcal{X}_{q,l}^n$ .
15:      Identify the element  $\widehat{\mathcal{K}}_{q,l}$  where  $\mathcal{X}_{q,l}^n$  belongs.
16:      Evaluate the solution value  $\widehat{\mathcal{T}}_{q,l}^n$  using the equation (20).
17:    end for
18:  end for
19:  Compute the element right-hand side  $r_i^n$  using the equation (16).
20:  Assemble the right hand-side vector  $\mathbf{r}^n$ .
21:  Solve the linear system in the equation (21).
22:  Calculate the solution  $\Theta_h^{n+1}$  at time  $t_{n+1}$  according to the equation (7).
23: end while

```

solution gradients are very high, the enriched semi-Lagrangian finite element method introduced in section 2 may require very fine meshes and high numbers of quadrature points to accurately capture these features. In the present study, to avoid uniform enrichments in the entire computational domain, we propose an multilevel adaptive algorithm for local enrichments to increase the efficiency of the proposed method. The key idea in this multilevel adaptive technique lies on refining the number of quadrature points $N_{l,Q}$ in mesh elements where the solution gradient generates high values and unrefine otherwise according to a given adaptation criterion. In practice, an error indicator along with a given tolerance are required to adapt the quadrature accordingly at each time step. For example, gradient-based error estimators have been widely used in the literature in h -adaptive finite element methods for solving incompressible Navier-Stokes equations, see [39, 40, 41, 42, 43, 44, 45, 46] among others. However, an initial coarse mesh to

compute a primary solution is needed in most of these gradient-based h -adaptive techniques for estimating the gradient errors. Therefore, error accumulations are expected in time because of the coarse mesh used in the approximation and also because of multiple interpolations between adaptive meshes, the computational cost becomes prohibitive. In the current work, we consider the normalized gradient of the temperature as an adaptive criterion for the local enrichments of each element in the computational domain defined by

$$\eta_{\mathcal{K}_l}^{n+1} = \frac{\|\nabla\Theta_{\mathcal{K}_l}^{n+1}\|}{\max_{j=1}^{N_e} \|\nabla\Theta_{\mathcal{K}_j}^{n+1}\|}, \quad (27)$$

where $\Theta_{\mathcal{K}_l}^{n+1}$ is the solution on the triangle \mathcal{K}_l at time t_{n+1} and $\|\nabla\Theta_{\mathcal{K}_l}^{n+1}\|$ is the L^2 -norm of the gradient of the solution on the element \mathcal{K}_l defined as

$$\|\nabla\Theta_{\mathcal{K}_l}^{n+1}\| = \left(\int_{\mathcal{K}_l} \nabla\Theta^{n+1} \cdot \nabla\Theta^{n+1} dx \right)^{\frac{1}{2}}. \quad (28)$$

Note that the error indicator (27) employs the gradient at the next time level t_{n+1} instead of the current time t_n . This implicit form is possible due to the semi-Lagrangian use method which approximates the solutions $\Theta_{\mathcal{K}_l}^{n+1}$ backwards in time as shown in (10). Hence, applying the gradient to the solution (11) we obtain

$$\nabla\Theta_{\mathcal{K}_l}^{n+1} = \sum_{i=1}^N \mathcal{T}_i^{n+1} \nabla\varphi_i(\mathbf{x}),$$

Thus,

$$\begin{aligned} \|\nabla\Theta_{\mathcal{K}_l}^{n+1}\|^2 &= \int_{\mathcal{K}_l} \nabla\Theta^{n+1} \cdot \nabla\Theta^{n+1} dx = \int_{\mathcal{K}_l} \left(\sum_{i=1}^N \mathcal{T}_i^{n+1} \nabla\varphi_i \right) \cdot \left(\sum_{j=1}^N \mathcal{T}_j^{n+1} \nabla\varphi_j \right) dx, \\ &= \sum_{i=1}^N \mathcal{T}_i^{n+1} \left(\sum_{j=1}^N \mathcal{T}_j^{n+1} \int_{\mathcal{K}_l} \nabla\varphi_i \cdot \nabla\varphi_j dx \right), \\ &= \left(\Theta_{\mathcal{K}_l}^{n+1} \right)^T \mathbf{S}_{\mathcal{K}_l} \Theta_{\mathcal{K}_l}^{n+1}, \end{aligned}$$

where $\Theta_{\mathcal{K}_l}^{n+1} = \left(\mathcal{T}_1^{n+1}, \dots, \mathcal{T}_N^{n+1} \right)^T$ are the values of Θ_h^{n+1} at the vertices of \mathcal{K}_l and $\mathbf{S}_{\mathcal{K}_l}$ is the elementary stiffness matrix evaluated at the element \mathcal{K}_l . Therefore, the temperature gradient at the element \mathcal{K}_l in (28) is calculated by

$$\|\nabla\Theta_{\mathcal{K}_l}^{n+1}\| = \left(\left(\Theta_{\mathcal{K}_l}^{n+1} \right)^T \mathbf{S}_{\mathcal{K}_l} \Theta_{\mathcal{K}_l}^{n+1} \right)^{\frac{1}{2}}. \quad (29)$$

Notice that the normalization in the criterion (27) is used to keep its values in the interval $[0, 1]$. Hence, the multilevel adaptive algorithm we propose in this study is carried out as follows.

Given a set of three real numbers $\{\varepsilon_m\}$ such that $0 = \varepsilon_0 < \varepsilon_1 < \varepsilon_2 < \varepsilon_3 < \varepsilon_4 = 1$. If an element \mathcal{K}_l in the computational mesh satisfies the condition

$$\varepsilon_m \leq \eta_{\mathcal{K}_l}^{n+1} \leq \varepsilon_{m+1}, \quad m = 0, 1, 2, 3,$$

then the element \mathcal{K}_l is enriched using the quadrature $(\mathbf{x}_{q,l}, \omega_{q,l})$, with $q = 1, 2, \dots, N_{Q_m}$. Note that the values of $\{\varepsilon_1, \varepsilon_2, \varepsilon_3\}$ are tolerances to be given by the user resulting into a three-level refining procedure. Algorithm 2 summarizes the steps used in the proposed multilevel adaptive enriched semi-Lagrangian finite element method for solving

the convection problem (4). Here, the number of levels m and the values of tolerances $\{\varepsilon_m\}$ in the above multilevel adaptive enriched semi-Lagrangian finite element method are problem dependent and their discussion is postponed for next section where numerical examples are discussed.

5. Numerical results

In this section several numerical examples are considered to examine the performance of the new enriched semi-Lagrangian finite element method proposed in this study. For the first example the exact solution is available, so that we can compute the relative L^1 -error and L^2 -error at time t_n as

$$L^1\text{-error} = \frac{\int_{\Omega} |\Theta_h^n - \Theta_{\text{exact}}^n| dx}{\int_{\Omega} |\Theta_{\text{exact}}^n| dx}, \quad L^2\text{-error} = \frac{\left(\int_{\Omega} |\Theta_h^n - \Theta_{\text{exact}}^n|^2 dx \right)^{1/2}}{\left(\int_{\Omega} |\Theta_{\text{exact}}^n|^2 dx \right)^{1/2}}, \quad (30)$$

where Θ_{exact}^n is the exact solution and Θ_h^n the numerical solution evaluated at the nodal point x_h and time t_n . Here, the CFL number is fixed and the time stepsize Δt is adjusted at each time step according to the stability condition as follows

$$\text{CFL} = \max_{x,y} \|\mathbf{u}\| \frac{\Delta t}{h}. \quad (31)$$

In our computations, all resulting linear systems of algebraic equations are solved using the conjugate gradient solver with incomplete Cholesky decomposition and stopping criteria set to $10^{-6}h$, which is small enough to guarantee that the algorithm truncation errors dominate the total numerical errors. All the computations were performed on an Intel® Core(TM) i7-7500U @ 2.70GHz with 16 GB of RAM. The CPU times presented in this section include all aspects of computational work including, mesh generation, calculation of characteristic curves, search-locate of departure points, assembling of finite element matrices, enrichment adaptation, and solution of linear systems.

5.1. Moving fronts problem

In this example we consider the problem of moving fronts in a squared domain in $\Omega = [0, 1] \times [0, 1]$ modeled by the transport-diffusion equation

$$\frac{\partial \Theta}{\partial t} + \mathbf{u} \cdot \nabla \Theta - \nu \nabla^2 \Theta = 0, \quad (32)$$

with a velocity field $\mathbf{u} = (u, v)^\top$ varying in time as

$$u(t, x, y) = \frac{-0.1e^{-A(t,x)} + 0.5e^{-B(t,x)} + e^{-C(t,x)}}{e^{-A(t,x)} + e^{-B(t,x)} + e^{-C(t,x)}}, \quad v(t, x, y) = \frac{-0.1e^{-A(t,y)} + 0.5e^{-B(t,y)} + e^{-C(t,y)}}{e^{-A(t,y)} + e^{-B(t,y)} + e^{-C(t,y)}},$$

where

$$A(t, z) = \frac{0.05}{\nu}(z - 0.5 + 4.95t), \quad B(t, z) = \frac{0.25}{\nu}(z - 0.5 + 0.75t), \quad C(t, z) = \frac{0.50}{\nu}(z - 0.375),$$

with $z = x$ or y . It is also easy to verify that the analytical solution of the problem (32) is given by

$$\Theta(t, x, y) = u(t, x, y)v(t, x, y).$$

Table 1: Results for the moving fronts problem obtained by the fixed and adaptive enriched semi-Lagrangian finite element methods using different structured meshes and different quadratures at time $t = 0.8$ using CFL = 3.5. Here, the CPU times are given in seconds.

h	N_Q	Fixed enrichment			Adaptive enrichment		
		L^1 -error	L^2 -error	CPU	L^1 -error	L^2 -error	CPU
$\frac{1}{32}$	12	0.06141	0.06851	0.34	0.06132	0.06878	0.29
	25	0.04521	0.05192	0.53	0.04636	0.05221	0.36
	52	0.03524	0.04471	0.79	0.03548	0.04501	0.38
	70	0.02873	0.04183	1.05	0.02904	0.04238	0.42
$\frac{1}{64}$	12	0.01589	0.01736	2.85	0.01596	0.01745	1.67
	25	0.01170	0.01307	3.85	0.01274	0.01314	1.77
	52	0.00887	0.01141	4.97	0.00898	0.01150	1.96
	70	0.00713	0.01010	6.75	0.00738	0.01061	2.11
$\frac{1}{128}$	12	0.00426	0.00431	28.12	0.00447	0.00441	14.20
	25	0.00297	0.00327	45.15	0.00299	0.00329	18.13
	52	0.00214	0.00287	78.97	0.00219	0.00290	26.67
	70	0.00181	0.00236	97.35	0.00183	0.00239	27.04

Table 2: Results for the moving fronts problem obtained by the conventional semi-Lagrangian finite element methods using different structured meshes at time $t = 0.8$ using CFL = 3.5. Here, the CPU times are given in seconds.

h	# elements	# nodes	L^1 -error	L^2 -error	CPU
$\frac{1}{32}$	512	1089	0.08952	0.09726	0.17
$\frac{1}{64}$	2048	4225	0.02953	0.04263	1.1
$\frac{1}{128}$	8192	166641	0.00859	0.00991	9.8

This problem has been previously solved in [54] using a moving finite element method and in [55] using a family of finite element alternating-direction methods combined with a modified method of characteristics. Initially, two separate fronts travel along the main diagonal of the computational domain at different speeds and eventually coalesce into one front for longer time. In our simulations, the initial and boundary conditions are defined by the exact solution, the diffusion coefficient $\nu = 5 \times 10^4$ and CFL = 3.5.

To examine the performance of the proposed approach we summarize in Table 1 the L^1 -error, L^2 -error and CPU times given in seconds. We present results obtained by the fixed and adaptive enriched semi-Lagrangian finite element methods using different structured meshes and different quadratures at time $t = 0.8$ using CFL = 3.5. For comparison, those results obtained using the conventional semi-Lagrangian finite element method are summarized in Table 2 for the same meshes. It is clear from the values of L^1 -error and L^2 -error that both the fixed and adaptive enrichments produce

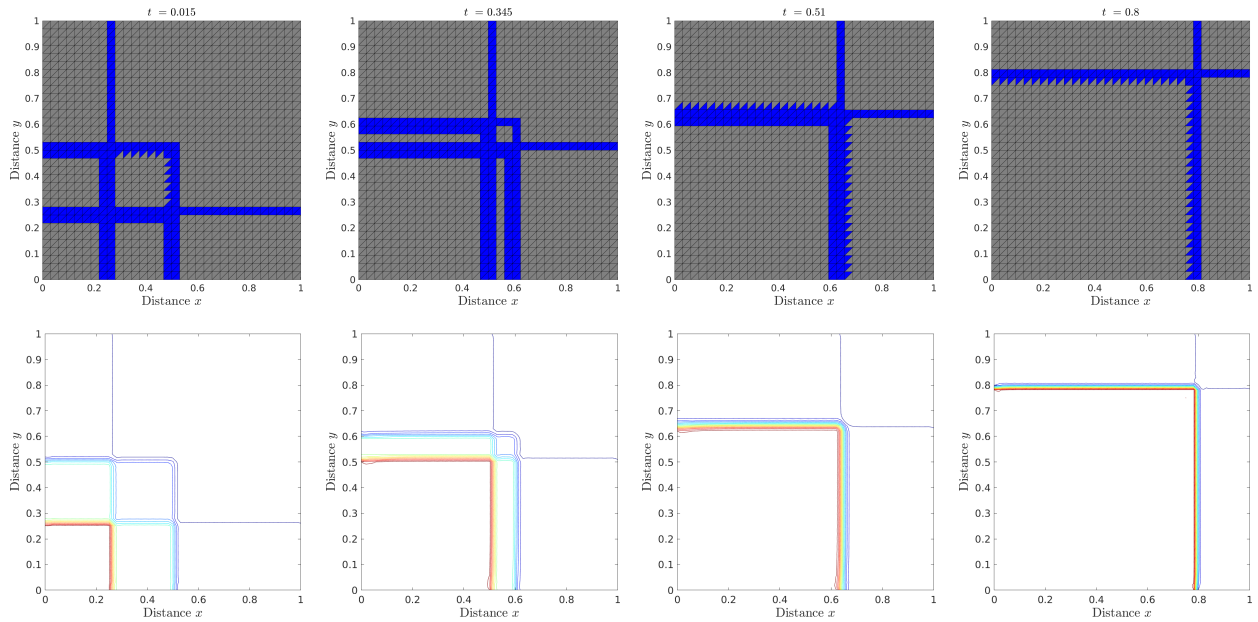


Figure 3: Adaptive quadrature points (first row) and solution contours (second row) for the moving fronts problem at time $t = 0.015$ (first column), $t = 0.345$ (second column), $t = 0.51$ (third column) and $t = 0.8$ (fourth column) on a structured mesh with $h = \frac{1}{64}$.

similar results with negligible differences for all considered meshes and numbers of quadrature points. However, compared to the conventional semi-Lagrangian finite element method, the enriched methods are far more accurate. Considering the q -refinement for this example, it is evident that by increasing the number of quadrature points in the simulations results in an improvement in the accuracy of the approximated solution for both fixed and adaptive enrichments. As expected, the adaptive enrichment approach is more efficient than its fixed counterpart, compare the computational costs in Table 1. Therefore, it is clear that the CPU times required for the fixed enrichment method are larger than the CPU times needed in the adaptive enrichment method. For instance, the adaptive enrichment method requires a CPU time about 60% less than the one required by the fixed enrichment method due to high demand of the global enrichments. This reduction in the computational cost becomes large when fine meshes are used in the simulations. As shown in the Table 1, using the fine mesh with $h = \frac{1}{128}$ the adaptive enrichment approach uses 72% of the computing time less than the fixed enrichment approach. However, the computational cost for the conventional approach in Table 2 is remarkably low compared to the enriched methods on the same configuration but the global accuracy of the conventional method is inferior to those achieved using the enriched methods.

In order to show the capability of the proposed adaptive enriched method to capture the moving sharp gradients in the approximated solution we display in Figure 3 the distribution of quadrature points and the corresponding 10 equi-distributed contourlines of the solution at four different times on a structured mesh with $h = \frac{1}{64}$. To highlight the element with and without enrichments, the elements of the computational mesh are colored to identify the number of quadrature points for each element. Therefore, in Figure 3 the enriched elements are colored in blue color and the

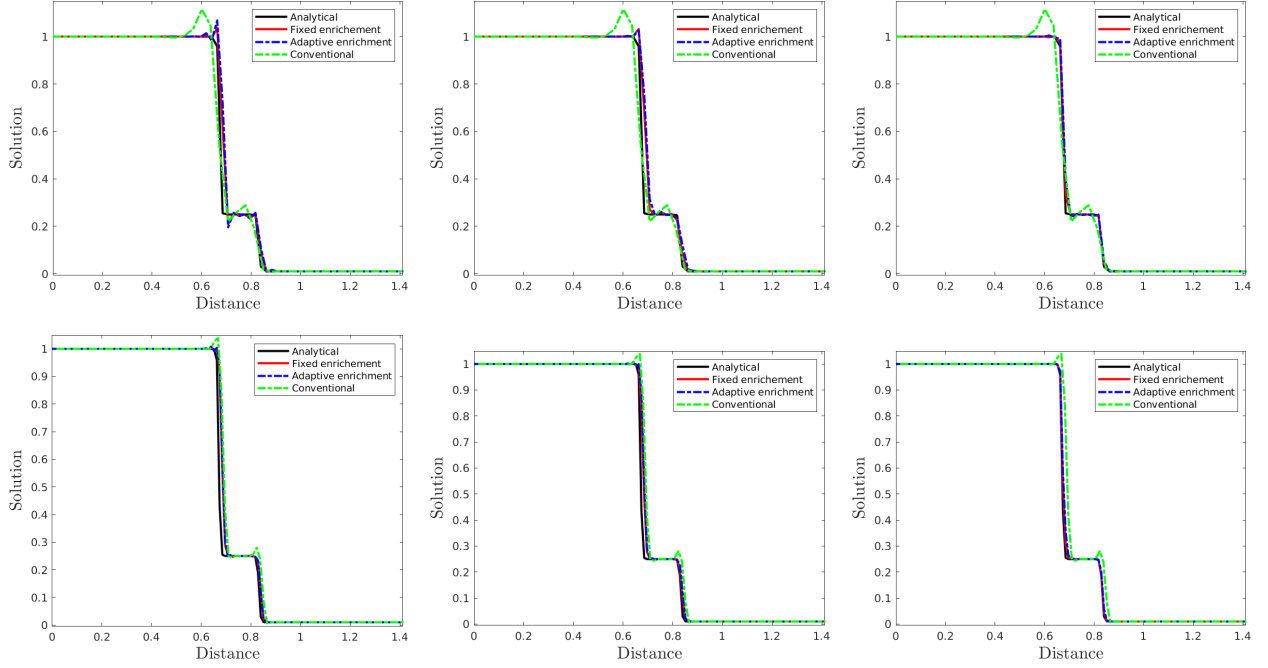


Figure 4: Cross-sections at the main diagonal $x = y$ obtained for the moving fronts problem at time $t = 0.8$ on a mesh with $h = \frac{1}{64}$ (first row) and $h = \frac{1}{128}$ (second row) using $N_{k,Q} = 12$ (first column), $N_{k,Q} = 25$ (second column) and $N_{k,Q} = 52$ (third column).

elements without enrichments are colored in gray color. In this test example a single-level adaptive enrichments is used according to a tolerance $\varepsilon_1 = 0.15$. In this simulation the elements subject to a sharp gradient are enriched with a number of quadrature points $N_{l,Q} = 52$ while the number of quadrature points is set to $N_{l,Q} = 6$ elsewhere. It is clear from the results in Figure 3 that the proposed enriched semi-Lagrangian finite element algorithm captures the steep gradients over time and the location of the enrichments follows the moving fronts with no distortion detected in the distribution of these enriched elements.

For comparison purpose, we present in Figure 4 cross-sections at the main diagonal $x = y$ of the results obtained using the fixed and adaptive enrichment methods on two meshes with $h = \frac{1}{64}$ and $h = \frac{1}{128}$. The results obtained using the conventional method and the analytical solutions are also included in this figure. It is clear that both the fixed and adaptive enrichment methods produce similar results which are close to the analytical solutions on both meshes. From the same results, it can be shown that the conventional semi-Lagrangian finite element method fails to accurately resolve this moving fronts problem, see the non-physical oscillations in the results obtained using the conventional method in Figure 4. Furthermore, the conventional method exhibits an excessive numerical diffusion compared to its enriched counterpart. The proposed enriched semi-Lagrangian finite element method resolves well this problem as it allows for a local refinement of quadrature points in mesh elements with sharp gradients in the computed solution while the computational mesh is kept fixed during the time integration process.

5.2. Transient buoyancy flow problem

This test example is used to assess the numerical performance of the proposed error indicator used for adaptive enrichments to resolve high gradients at scales of the mesh which occur in the buoyancy flows. Here, we solve the coupled flow-transport problem proposed in [56] as a benchmark for numerical methods of incompressible buoyancy flows. The flow problem consists of the transport of a hot plume in a cold fluid placed in a squared cavity. Here, we solve the coupled equations (3) in the unit squared domain $\Omega = [0, 1] \times [0, 1]$ with a light plume placed in the lower half of the studied cavity $[0.375, 0.625] \times [0.25, 0.5]$. The plume has a void temperature $\Theta = 1$ and the surrounding medium has a temperature $\Theta = 0$. At initial time $t = 0$, the fluid is at rest and no-slip boundary conditions for the velocity and adiabatic boundary conditions for the temperature are imposed. In our simulation, $Pr = 5$, $Re = 10^3$ and $Ri = 1$, and a fixed unstructured mesh is intentionally selected to be sufficiently coarse, being composed of 3100 elements only with 6343 nodes for velocity/temperature and 1622 for pressure. Initially, the number of quadrature points is set to $N_{l,Q} = 6$ in all elements in the computational mesh and tolerances of $\varepsilon_1 = 0.07$, $\varepsilon_2 = 0.15$ and $\varepsilon_3 = 0.3$ are used for the three-level adaptive enrichments. In general, any number of enrichment levels can be used in the proposed algorithm and it is up to the user to decide on how many levels should be used. For the considered flow problems, we have found that increasing the number of enrichment levels beyond four results in no further improvements in the obtained results.

In Figure 5 we present results for the distribution of quadrature points, velocity fields and isotherms at four different times $t = 1, 2.43, 3.6$ and 4.89 using a CFL number fixed to 2.5. For the considered values of Re and Ri , the buoyancy force increases the shear stresses on the cavity walls which yields an increase in the velocity field. These wall effects slow the transport of the plume towards the upper cavity wall allowing the plume to preserve its compact shape during the whole simulation period. These results are in good agreement with those results reported in the literature, see for example [56]. It is also clear from the results in Figure 5 that the high solution gradients are perfectly captured at the considered times despite that from a certain time the filaments become closer to each other. The interface has been accurately captured in our computations using the adaptive enrichments. Furthermore, this test example demonstrates the high resolution of the adaptive enriched semi-Lagrangian finite element method, which can refine the quadrature points in the vicinity of the interface and it reduces the computational effort without sacrificing the accuracy. For comparison reasons, we also display in Figure 6 the isotherms obtained at time $t = 4.3$ using fixed, adaptive enriched methods, the conventional method and a reference solution obtained on a fine mesh with 32768 elements and 66049 nodes. The time evolution of the kinetic energy for this problem is also compared in Figure 6 to the results reported in [56]. The performance of our adaptive enrichment procedure is very attractive since the computed solutions remain stable without nonphysical oscillations appearing in the vicinity of sharp gradients in the interface. These features are resolved in our adaptive enriched semi-Lagrangian finite element method without requiring small time steps or very fine meshes. It should also be noted that, we use a single fixed mesh in our adaptive enriched method and the gradient is evaluated from the known solution at next time level obtained by backtracking along the characteristic curves. Therefore, a considerable reduction in the computational cost was ensured compared

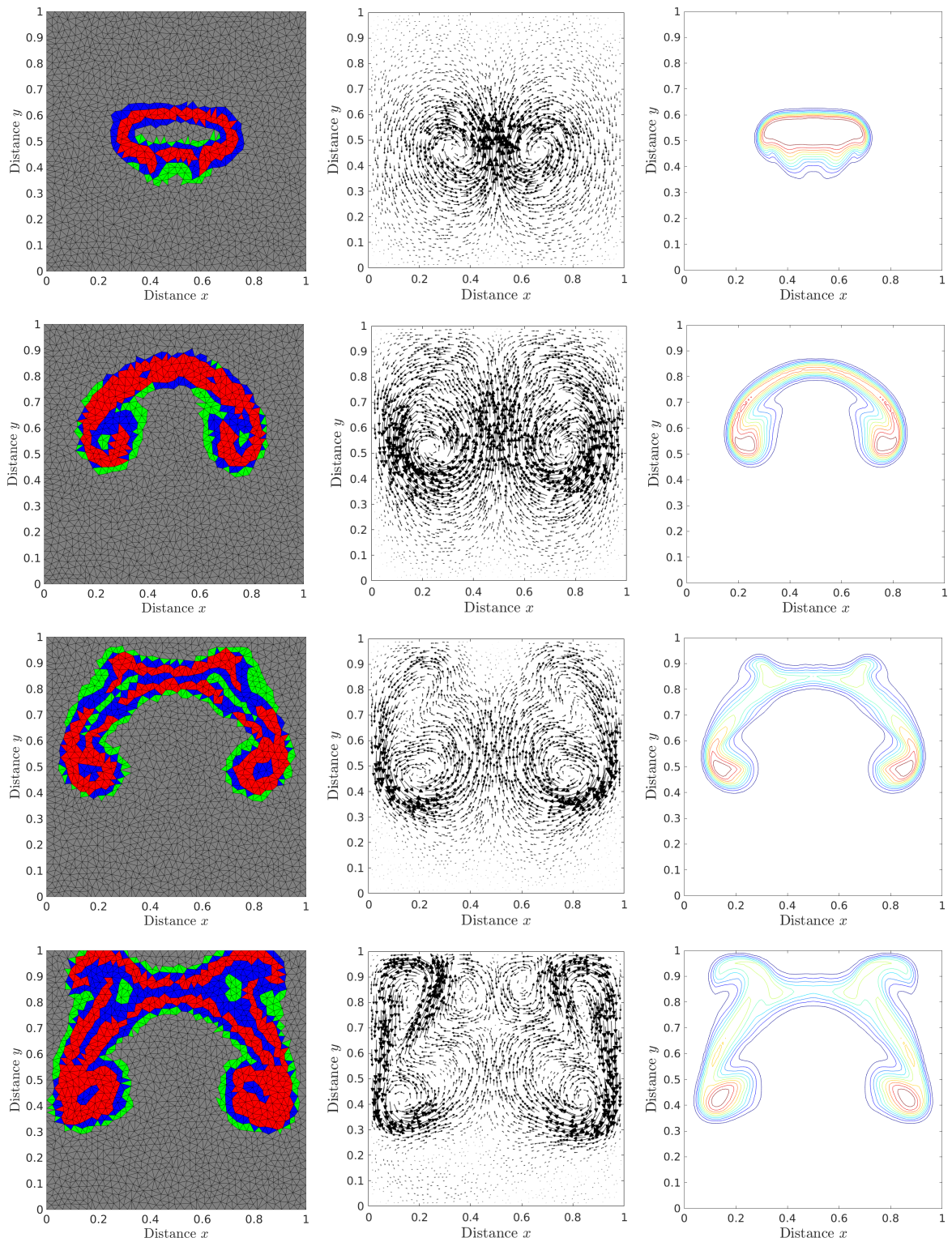


Figure 5: Adaptive quadrature points (first column), velocity fields (second column) and isotherms (third column) for the transient buoyancy flow at time $t = 1$ (first row), $t = 2.43$ (second row), $t = 3.6$ (third row) and $t = 4.89$ (fourth row) on an unstructured mesh with 3100 elements.

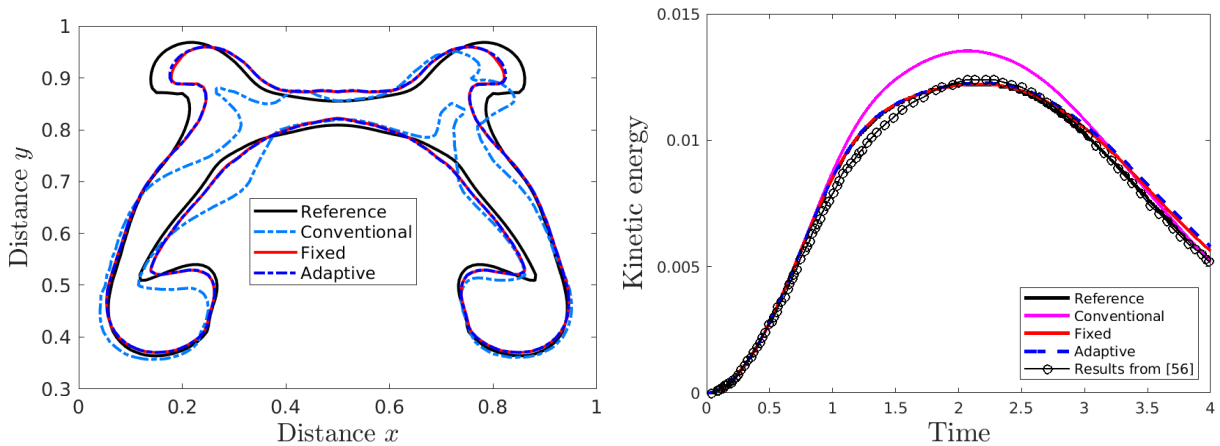


Figure 6: Comparison of isotherms at time $t = 4.3$ (left) and time evolution of the kinetic energy (right) obtained for the transient buoyancy flow using different methods.

to the calculation of gradient in h -adaptive methods. In such methods, two meshes are needed for each time step for which a coarse mesh is used to calculate the gradient whereas the refined mesh is used to compute the solution. Thus, an additional cost is added which is not the case in our adaptive enrichment algorithm. Note that the reference solutions have been obtained using highly refined meshes for which the number of degrees of freedom are far larger than those used in the enriched solutions. Therefore, the discrepancies between the enriched and reference solutions are expected but refining the mesh in the enriched method would converge to the reference solutions. Here, even the used mesh is coarse, the obtained results show a significant improvement in accuracy and efficiency compared to the conventional finite element method but by refining the mesh, the obtained results converge to the reference solutions.

5.3. Thermal flow past a cylinder

To illustrate the capability of the proposed multilevel adaptive enriched semi-Lagrangian finite element method for complex problems, we consider the coupled transport-flow problem of a viscous thermal flow past a circular cooled cylinder subject to a vertically upward laminar flow. The characteristics of vortex shedding behind circular cylinders or similar two-dimensional bluff bodies have been widely used in the literature to test the accuracy of numerical methods for the incompressible Navier-Stokes equations, see for example [57, 58, 59, 10]. The geometry and the mesh used in our simulations for this example are shown in Figure 7. Here, a fixed circular cylinder with diameter $D = 1$ is placed in a vertical flow with velocity $u_\infty = 1$ and temperature $\Theta_\infty = 1$. The Reynolds number is defined as $Re = Du_\infty/\nu$, where ν is the kinematic viscosity. In our simulations, the Prandtl number $Pr = 0.71$, the Richardson number $Ri = 1$ and two values of Reynolds numbers $Re = 100$ and $Re = 200$ are considered. The CFL number is fixed to 3.5 and we use the unstructured triangular finite element P_2/P_1 mesh shown in Figure 7 in the simulations. This mesh is composed of 3149 elements with 6802 velocity/temperature nodes and 1804 pressure nodes. The major objective of this test case is to demonstrate that proposed multilevel adaptive enrichments are capable to accurately

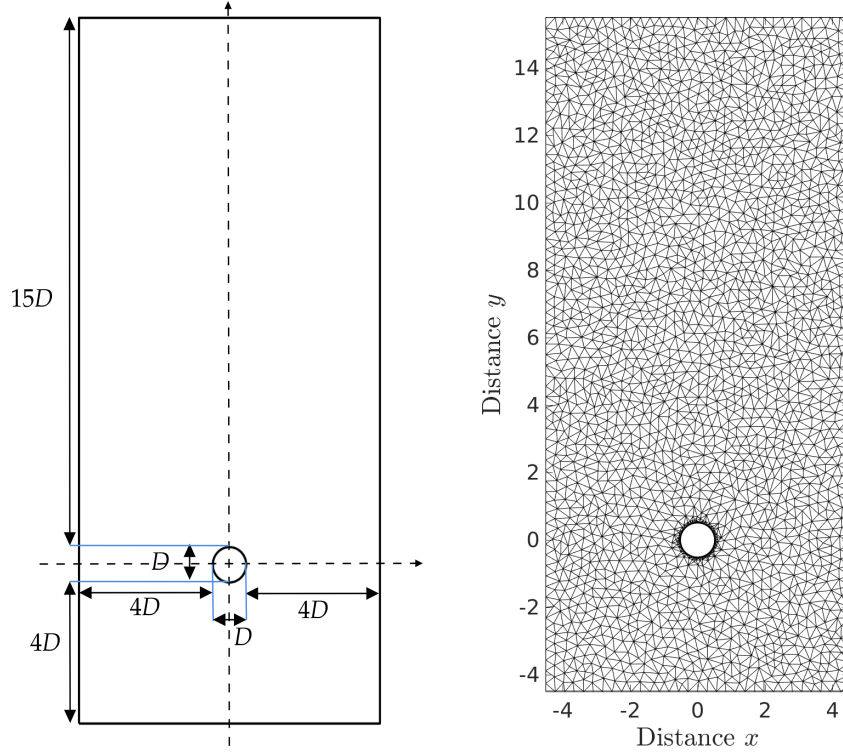


Figure 7: Configuration of the computational domain (left) and computational mesh (right) used for the problem of thermal flow past a cylinder.

capture sharp gradients and vortex shedding in the approximated solutions with inexpensive computational costs. Here, we investigate a three-level adaptive enrichments with tolerances $\varepsilon_1 = 0.04$, $\varepsilon_2 = 0.15$ and $\varepsilon_3 = 0.25$. Initially, the number of quadrature points is $N_{l,Q} = 6$ in each element in the mesh, then this number is modified according to Algorithm 2 using $(N_{l,Q} = 12, N_{l,Q} = 52, N_{l,Q} = 70)$.

Figure 8 depicts the velocity fields, the distribution of quadrature points using three-level adaptive enrichments and the temperature snapshots obtained at five different instants $t = 3.9, 7.3, 10, 14.9, \text{ and } 156.1$. For a better illustration, different colors are used to identify the mesh element with quadrature points for each level of enrichments in the computational mesh. It should also be noted that the results obtained using the single-level and two-level enrichments are not included for this example because these results overlap those obtained using the three-level enrichments. For the considered conditions, the flow past the cylinder exhibits eddies with different magnitudes and the recirculating zones behind the cylinder increases within the simulation time. Therefore, large vortices and thermal fronts appeared in the domain yield elements with steep gradients in the computational mesh to be enriched. The proposed multilevel adaptive enrichment method accurately captures these sharp gradients in the numerical solution and correctly enriches their associated elements. Note that this class of flows past solid bodies is unsteady in time and adaptation techniques are highly recommended to reduce the computational costs. From the results shown in Figure 8, it is apparent that the proposed multilevel adaptive enriched semi-Lagrangian finite element method resolves this coupled flow-transport

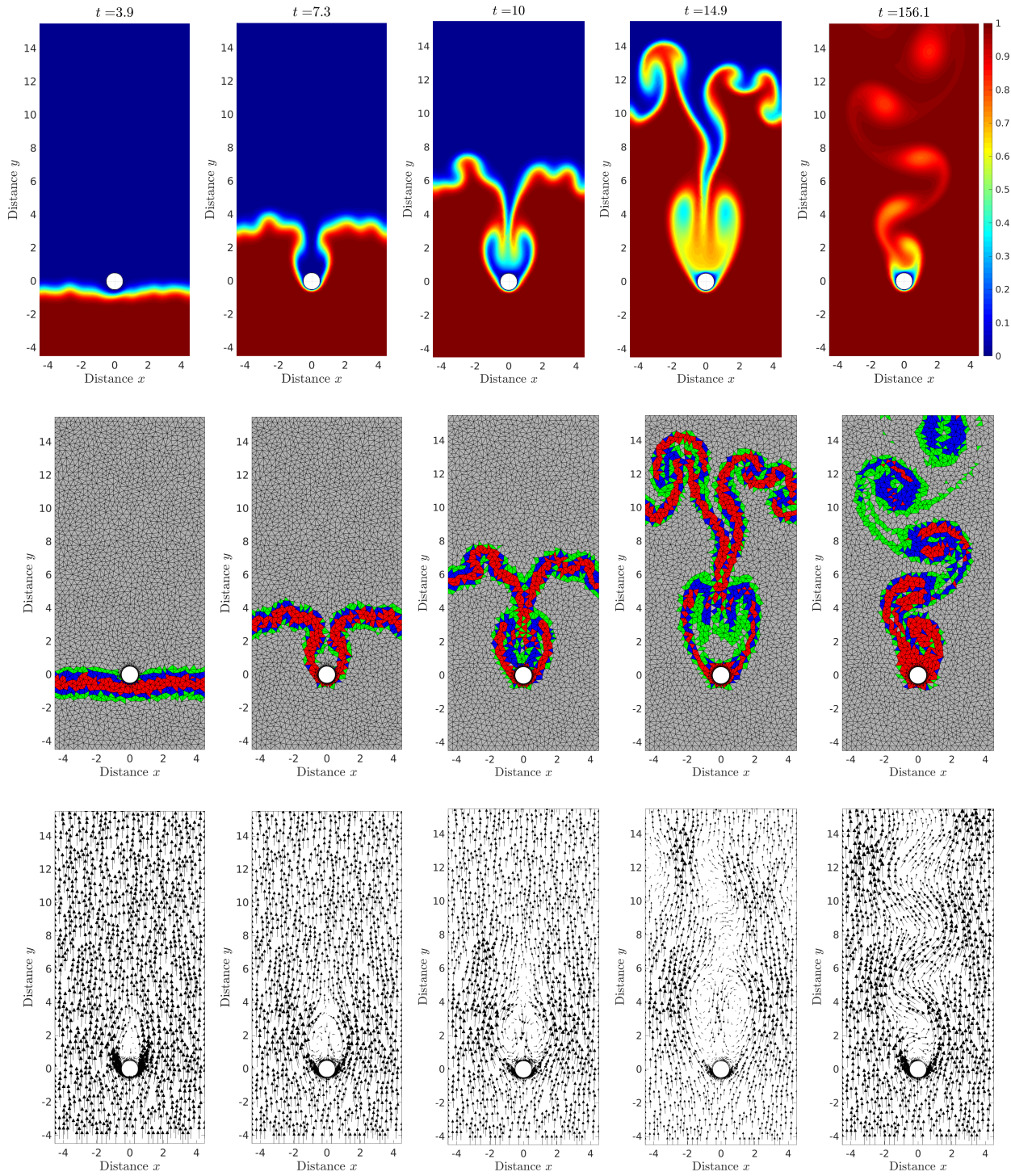


Figure 8: Temperature snapshots (First row), adaptive quadrature points (second row) and velocity field (third row) for flow past cylinder with $Re = 100$ at time $t = 3.9$ (first column), $t = 7.3$ (second column), $t = 10$ (third column), $t = 14.9$ (forth column) and $t = 156.1$ (fifth column).

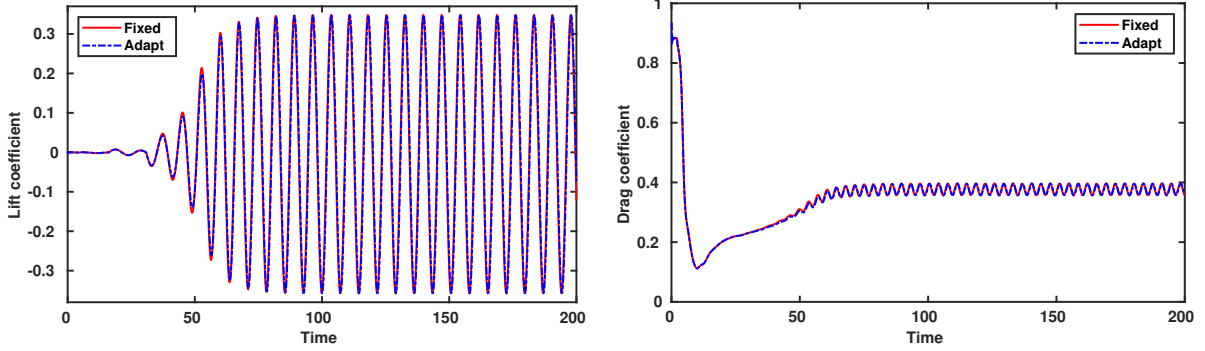


Figure 9: Lift and drag coefficients for the flow past a circular cylinder at Reynolds number $Re = 100$ obtained using fixed and adaptive enrichments.

problem accurately by adapting the quadrature points where it is needed with different densities and different structures according to the sharpness of solution gradients. Moreover, the proposed multilevel adaptive method capture the heat transport and the flow eddies around the cylinder very well. These results demonstrate the efficiency of our adaptation criterion which is approximated backward thanks to the modified method of characteristics.

For comparison purposes, we quantify the results of this coupled flow-transport past a cylinder by evaluating the force coefficients at each time step as

$$\text{Lift} = \oint_0^{2\pi} \left(-pn_x + \nu \frac{\partial u}{\partial x} \right) dx, \quad \text{Drag} = \oint_0^{2\pi} \left(-pn_y + \nu \frac{\partial v}{\partial y} \right) dx,$$

where $(n_x, n_y)^\top$ is the outward unit normal vector on the cylinder surface. In Figure 9 we display the time evolution of the lift and drag coefficients obtained using the fixed and three-level enrichments. Initially, the lift coefficient starts from zero and rapidly oscillates later with increasing amplitudes. Similarly, after an initial stabilization phase, the oscillatory behavior in the drag coefficient exhibits a steady feature in the considered time period. As expected for this type of flow problems, the vortex shedding from the circular cylinder generate fluctuations in the lift and drag forces. As can be seen in Figure 9, there is no noticeable differences between the results obtained for these forces using the fixed and adaptive enrichments. For the considered flow parameters, fluctuations with higher frequencies are detected in the drag coefficient compared to the lift coefficient. The periodic behavior of the lift coefficient should also be noted in the results displayed in Figure 9. The results obtained using our multilevel adaptive enriched semi-Lagrangian finite element method show good agreement with all flow variables reported in the literature, see for instance [30, 10, 60, 61].

To further quantify the periodic behavior of the lift coefficient, we calculate the dimensionless Strouhal number as $St = DT/u_\infty$, with T is the time period. The Strouhal number has been widely used in experimental works for this class of flows around rigid bodies, see [30, 60] among others. In Table 3 we summarize the Strouhal numbers, averaged iterations in the conjugate gradient algorithm and CPU times at for two Reynolds numbers $Re = 100$ and $Re = 200$ using fixed and adaptive enrichments on Mesh I and Mesh II at time $t = 200$. Here, Mesh I contains 3149 elements with 6802 nodes for the velocity/temperature solutions and 1804 nodes for the pressure solution whereas,

Table 3: Strouhal numbers, averaged iterations and CPU times (in minutes) for the flow past cylinder at Reynolds numbers $Re = 100$ and 200 obtained using adaptive enrichments.

Mesh	# elements	$Re = 100$						$Re = 200$					
		Fixed enrichment			Adaptive enrichment			Fixed enrichment			Adaptive enrichment		
		St	Iter	CPU	St	Iter	CPU	St	Iter	CPU	St	Iter	CPU
Mesh I	3149	0.13780	2.095	779	0.13798	2.100	265	0.14606	2.579	844	0.14537	2.581	281
Mesh II	4955	0.14042	1.782	882	0.14012	1.782	341	0.15363	2.021	946	0.15346	2.021	356



Figure 10: Schematic map of the Mediterranean Sea along with relevant locations.

Mesh II contains 4955 elements with 10359 nodes for the velocity/temperature solutions and 7657 nodes for the pressure solution. As expected, the results obtained for the Strouhal number St using the adaptive enrichments are similar to those given by the fixed enrichments for both considered Reynolds numbers and meshes. Moreover, the adaptive procedure reduces the number of quadrature points about 4.5 times. It can be shown from the table 3 that the adaptive enrichments can achieve the same accuracy of the fixed enrichments using a CPU about 60% than the one needed in the fixed enrichments for all meshes and Reynolds numbers.

5.4. Heat transport in the Mediterranean Sea

Our final test example consists of a problem of heat transport in the Mediterranean Sea using the coupled flow-transport equations (3). The Mediterranean Sea of 4000 km west-east length and 1500 m of averaged depth is a semi-enclosed basin, naturally connected to the large Atlantic ocean basin by the Strait of Gibraltar which enables and at the same time limits this dynamic communication between the basins, see the map in Figure 10. The budgets of heat and freshwater surface in the Mediterranean basin are negative. However, about 90% of these deficits of freshwater

Table 4: Mesh statistics, values of the kinetic energy and the total averaged temperature and at time $t = 10.5$ days, and computational times for the considered meshes in the problem of heat transport in the Mediterranean Sea using $R_i = 0$ and $R_i = 1$. The CPU times are given in seconds.

	# elements	# P_2 nodes	# P_1 nodes	$R_i = 0$			$R_i = 1$		
				Energy	Averg Θ	CPU	Energy	Averg Θ	CPU
Mesh A	14217	33759	9757	4.665E+06	5.411E+07	558	4.233E+06	3.188E+07	632
Mesh B	18827	42979	12062	3.484E+06	5.164E+07	1020	3.551E+06	2.939E+07	1119
Mesh C	27376	60078	16337	2.828E+06	4.887E+07	1668	3.705E+06	2.598E+07	1754
Mesh D	47325	100015	26330	2.559E+06	4.718E+07	2646	3.168E+06	2.649E+07	2801

and heat are balanced by the Atlantic waters that enter through the strait of Gibraltar, see for instance [62]. This inflow is warmer and fresher (15.4°C , 36.2 psu) while the outflow to the Atlantic basin is cooler and saltier 13°C , 38.4 psu , see [63] among others. In practice, the heat transport is affected by the circulation of the Sea which is forced by the water flow exchange through various straits (Gibraltar, Otrano sicily), by wind stress, and by buoyancy forces at the surface, see for example [64]. Note that the validity of using the two-dimensional Navier-Stokes/Bousinesq equations is supported by the geometry of the Mediterranean Sea and the temperature differences between the Mediterranean and the Atlantic waters. Hence, we solve the equations (3) in the computational domain illustrated in Figure 10 using four different meshes shown in Figure 11. The system is assumed initially at warm rest and at the left and right boundary regions we use cold temperature $\Theta = 17^\circ\text{C}$ and hot temperature $\Theta = 23^\circ\text{C}$, respectively. All coastlines of the Mediterranean Sea are considered as adiabatic boundaries. For the water flow, a well developed velocity profile with a maximum velocity $u_\infty = 0.54\text{ m/s}$ is imposed at the western entrance of the Sea. This profile corresponds to the annual mean of the Atlantic input flux and it is also comparable to the main semidiurnal component M_2 , see for instance [65, 64, 63]. In our simulations, we consider a three-level adaptive enrichment with tolerances $\varepsilon_1 = 0.07$, $\varepsilon_2 = 0.13$ and $\varepsilon_3 = 0.3$ for which the initial number of quadrature points is set to $N_{l,Q} = 6$ in each element and this number is refined according to Algorithm 2 using $(N_{l,Q} = 12, N_{l,Q} = 25, N_{l,Q} = 52)$. Both uncoupled ($Ri = 0$) and coupled ($Ri = 1$) flow-transport cases are considered for this problem using $Pr = 7.15$, $Re = 10^4$ and a fixed CFL = 5.5 The obtained results are also compared to those computed using the conventional semi-Lagrangian finite element method. Our objective for this example is twofold, on one hand to assess the capability of our multilevel adaptive enriched semi-Lagrangian finite element method to accurately handle complex geometries and on the other hand to develop robust numerical tools to efficiently study heat transport the Mediterranean Sea.

In our simulations for this problem, we consider a series of unstructured meshes with triangular finite elements as depicted in Figure 11 with the corresponding number of elements listed in Table 4. In Figure 12 we illustrate the cross-sections of the temperature at the line connecting the two points A and B shown in Figure 10 for $Ri = 0$ and $Ri = 1$ using the considered meshes at time $t = 10.5$ days. The selected points A and B are located in the Mediterranean

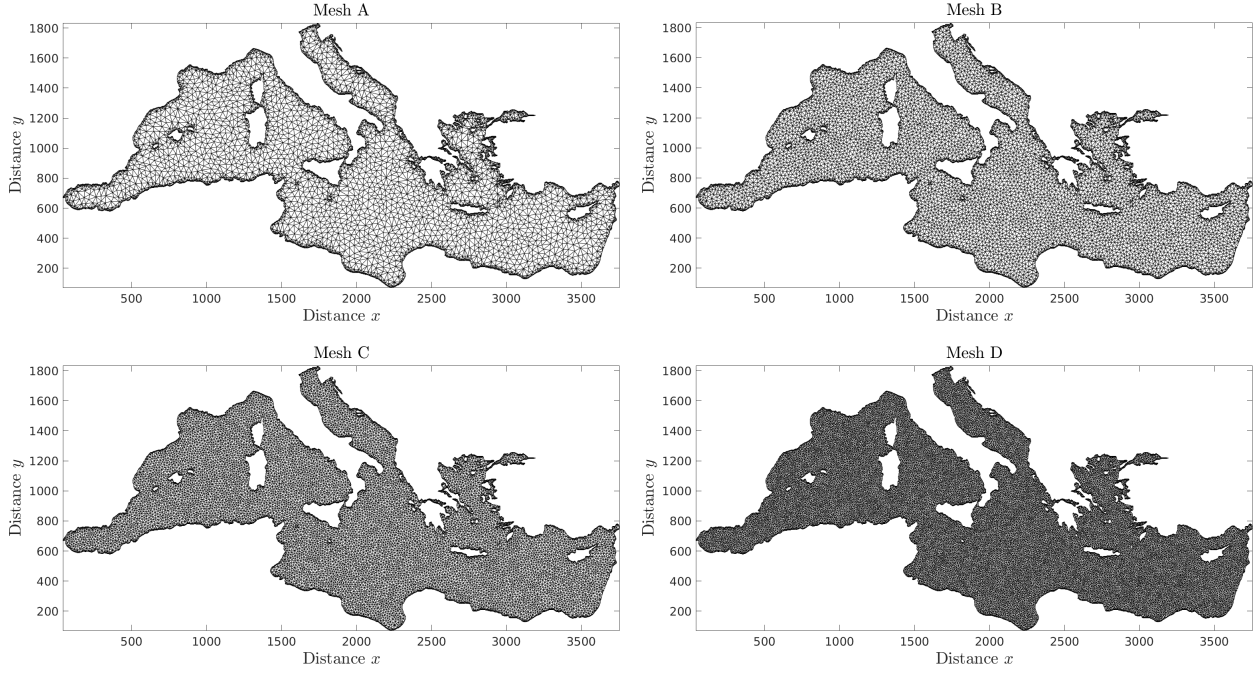


Figure 11: Finite element meshes used for the problem of heat transport in the Mediterranean Sea.

Sea at $(1517 \text{ km}, 788 \text{ km})$ and $(1643 \text{ km}, 868 \text{ km})$, respectively. It is easy to verify that solutions obtained for both values of Ri using the coarse Mesh A are less accurate than those obtained using the fine Mesh D. Refining the density of elements in the computational domain, the results for the Mesh C and Mesh D are roughly similar. This confirms the mesh convergence in the proposed multilevel adaptive enriched semi-Lagrangian finite element method for this test example. To further quantify the results for this mesh convergence study we summarize in Table 4 the computational times, the averaged temperature volume and the total kinetic energy obtained at time $t = 10.5$ days using the considered meshes and values of Ri . Here, the total kinetic energy and the averaged temperature volume are defined as

$$\frac{1}{2} \int_{\Omega} (u^2(t, \mathbf{x}) + v^2(t, \mathbf{x})) \, d\mathbf{x} \quad \text{and} \quad \frac{1}{|\Omega|} \int_{\Omega} \Theta(t, \mathbf{x}) \, d\mathbf{x},$$

respectively. As can be observed, there is little difference between the results obtained for the total kinetic energy and the averaged temperature volume on the last two meshes Mesh C and Mesh D. For example, the discrepancies in values of the total kinetic energy and the averaged temperature volume on Mesh B and Mesh C are less than 19% and 5%, respectively. These differences become less than 10% and 3% on meshes Mesh C and Mesh D. Therefore, bearing in mind the slight change in the results from Mesh C and Mesh D at the expense of rather significant increase in CPU times, the Mesh C is believed to be adequate to obtain the results free of grid effects. Hence, the results presented herein are based on the Mesh C.

Figure 13 displays the velocity fields, streamlines, temperature snapshots and distribution of quadrature points

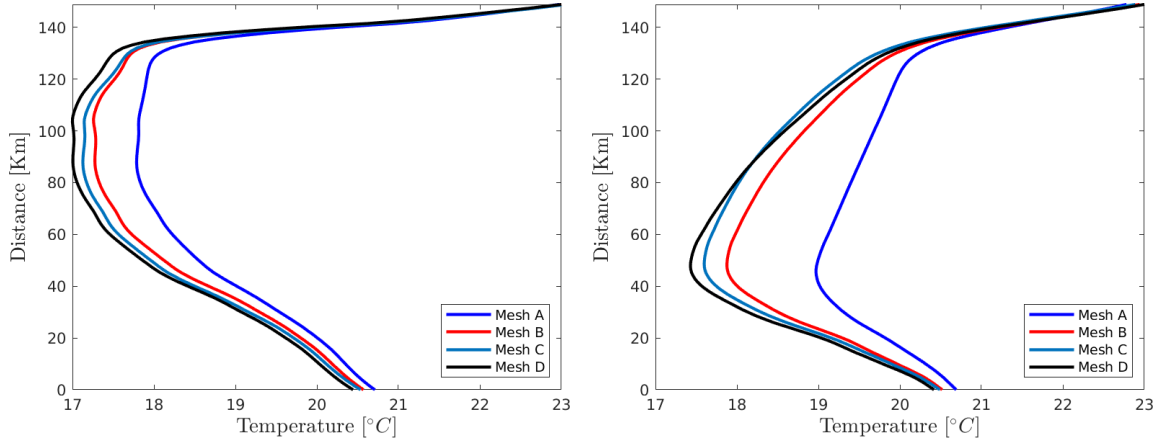


Figure 12: Cross-sections of the temperature for the problem of heat transport in the Mediterranean Sea at time $t = 10.5$ days using four different meshes with $Ri = 1$ (left) and $Ri = 0$ (right).

using three-level adaptive enrichments with $Ri = 0$ at five different times $t = 1$ day , 2.5 days, 5 days, 8 Days and 10.5 days. Those results obtained for the coupled situation with $Ri = 1$ are displayed in Figure 14. At earlier simulation times and for both values of Ri , the cold Atlantic front entering the Mediterranean Sea through the Gibraltar strait starts to develop and it is transported later on by the flow at far exit of the Sea. A stronger interaction between the heat transfer and the water flow is detected across the Mediterranean Sea for the case with $Ri = 1$ than for $Ri = 0$. It can be clearly seen that the complicated temperature and flow structures being captured by the proposed multilevel adaptive enriched semi-Lagrangian finite element method. For example, decrease and increase of the strengths of flow vortices with time can be seen in Figure 13 and Figure 14. Inside these vortices, there is a more complex vortex pattern. From this figures it can also be seen that these vortices and the high gradients in the moving thermal plume are successfully captured by our adaptive approach and the quadrature points are distributed in areas with the prescribed tolerances according to the desired three-level enrichments in the computational domain. Here, three different colors are used illustrate the distributions of quadrature points such that green color is used for the first level, blue color for the second level and red color for the third level, whereas gray color is used for elements with smooth solutions and low thermal gradients. As expected, denser quadrature points are detected for the three-level adaptive enrichments. From the computed results for this example under the considered flow conditions, the thermal front is mainly transported towards the African coast. The cold Atlantic front follows the stream induced by the mean flow entering the Mediterranean Sea through the Gibraltar strait. During its convection, the heat transport alerts the flow structure developing recirculation zones with different frequencies and magnitudes in several regions in the Mediterranean Sea. The large downstream recirculation zone in the eastern Mediterranean is mainly due to the temperature differences at this region. In summary, the heat transport is captured accurately, the flow field is resolved reasonably well, and the temperature front is shape preserving. All these features have been achieved using time steps larger than those required for Eulerian-based finite element methods in convection-dominated flows.

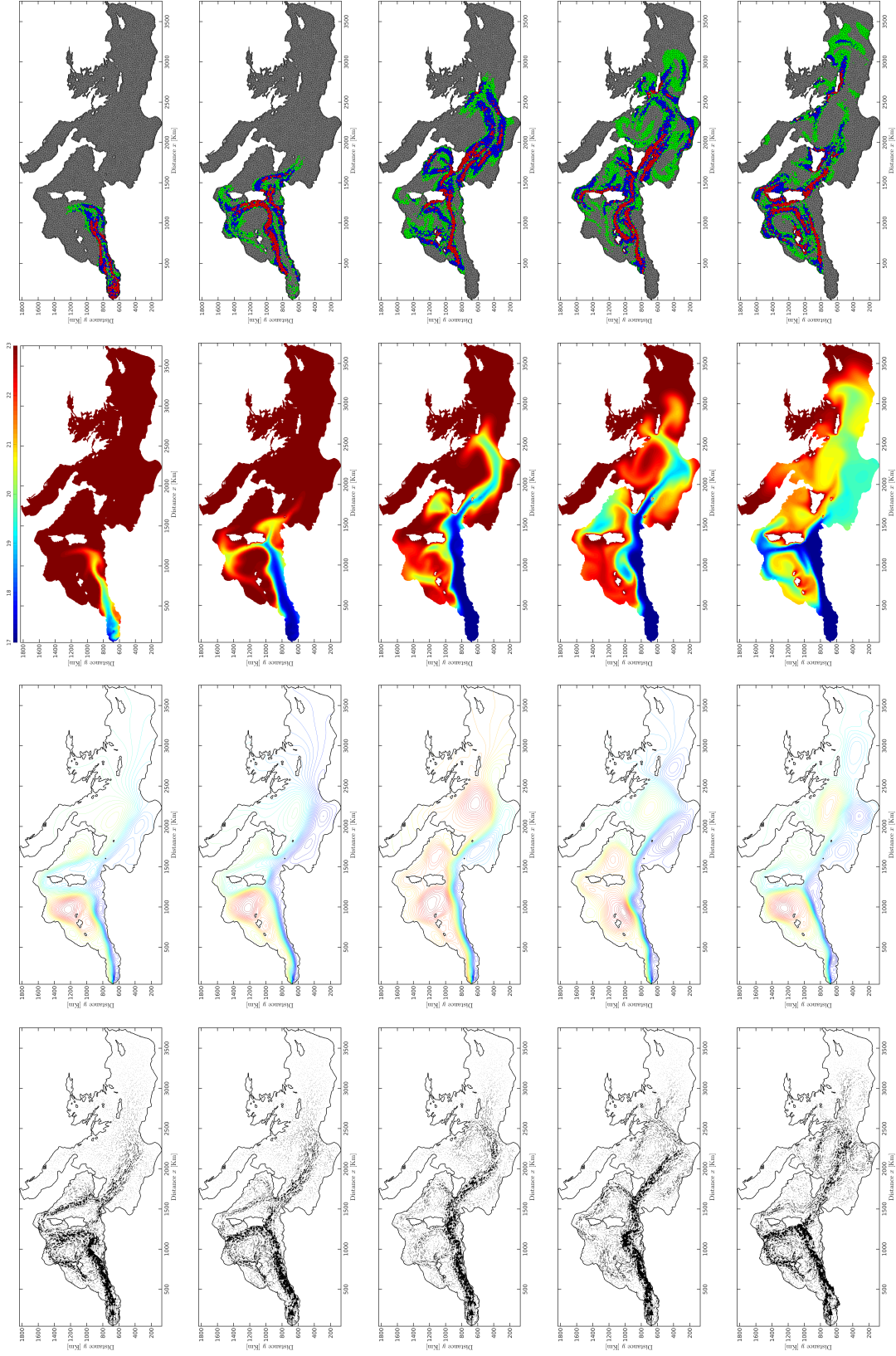


Figure 13: Velocity fields (first column), streamlines (second column), temperature snapshots (third column) and distributions of quadrature points (fourth column) for the problem of heat transport in the Mediterranean Sea with $Ri = 0$ at time $t = 1$ day (first row), $t = 2.5$ days (second row), $t = 5$ days (third row), $t = 8$ days (fourth row) and $t = 10.5$ days (fifth row).

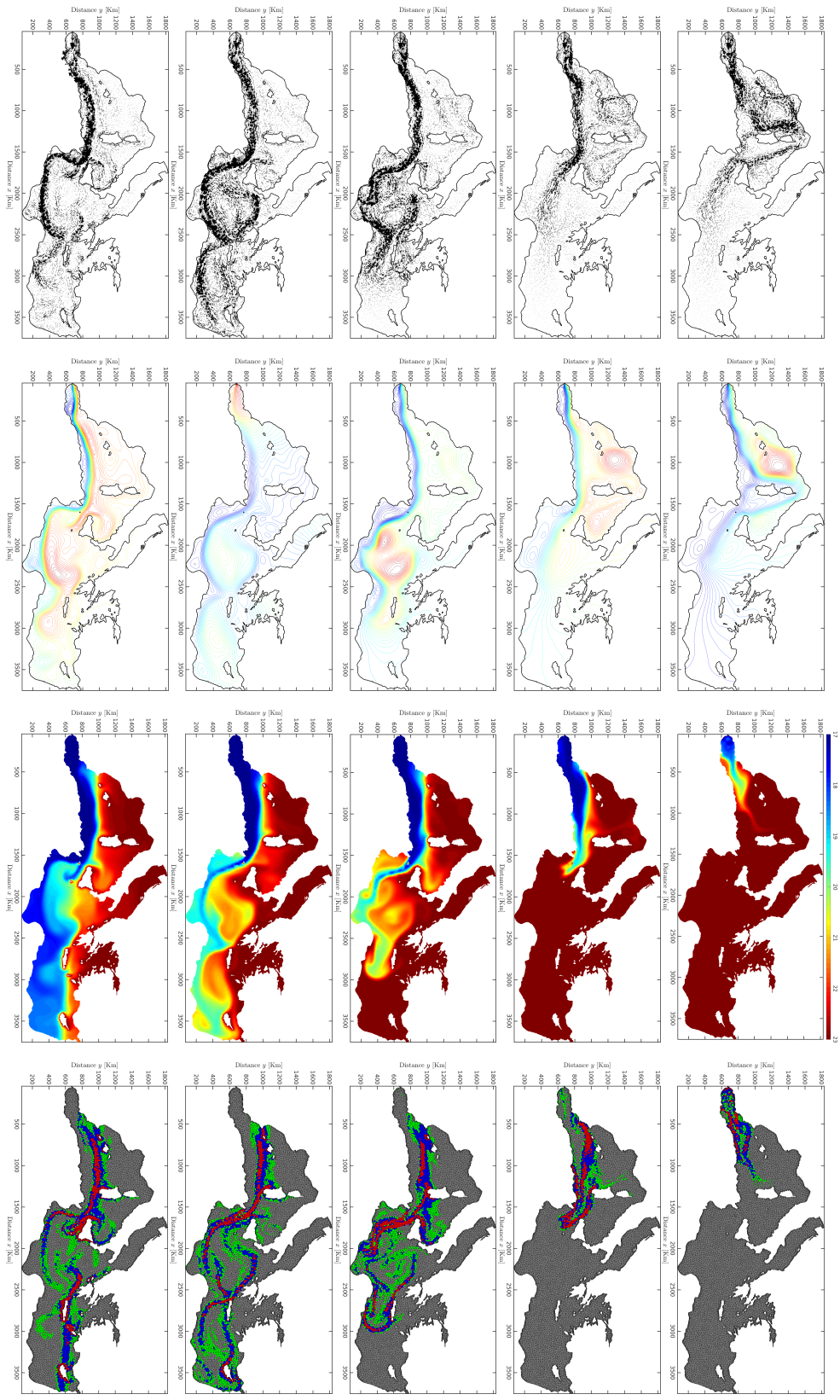


Figure 14: Same as Figure 13 but using $Rf = 1$.

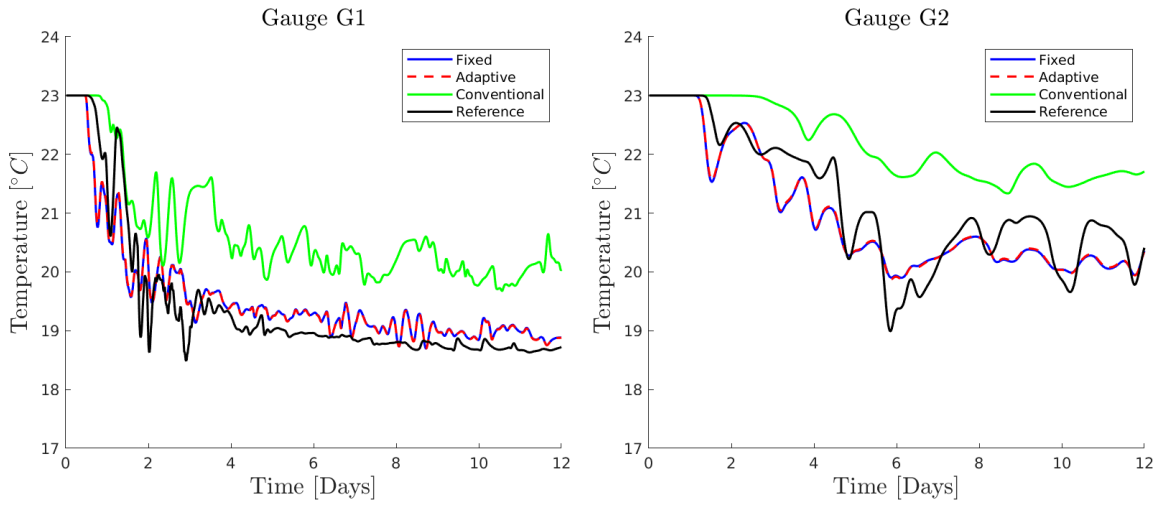


Figure 15: Time evolution of the temperature at the gauge G1 (left) and gauge G2 (right) for the problem of heat transport in the Mediterranean Sea with $Ri = 0$.

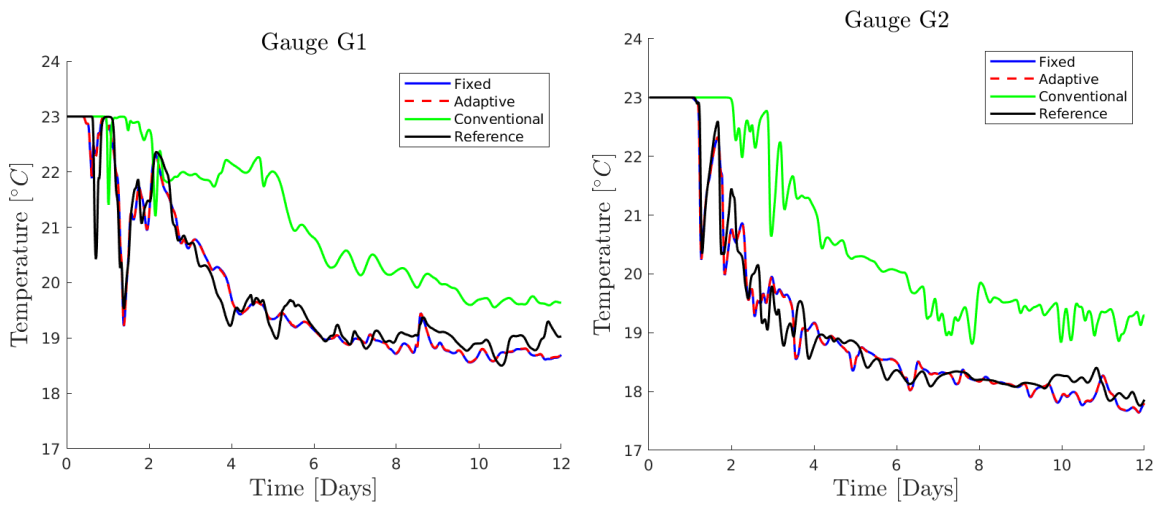


Figure 16: Same as Figure 15 but using $Ri = 1$.

Comparisons between results obtained using the conventional method, the fixed and adaptive enrichments have also carried out for this test example. To this end, the temperature is monitored at the two gauges G1 and G2 located respectively at $(1936.7 \text{ km}, 545.2 \text{ km})$ and $(2886 \text{ km}, 400 \text{ km})$ in the Mediterranean Sea as shown in Figure 10. Figure 15 depicts the time evolution of the temperature at the gauges G1 and G2 obtained using the fixed with $N_{l,Q} = 52$ and the three-level adaptive enrichments for the uncoupled case with $Ri = 0$. Those results obtained for the coupled case with $Ri = 1$ are presented in Figure 16. Reference solutions obtained using fixed enrichments with $N_{l,Q} = 52$ on a fine mesh with 47327 elements are also included in these figures. For both cases with $Ri = 0$ and $Ri = 1$, the

temperature exhibits fluctuations in its time evolution at the selected gauges G1 and G2 but bounded between the cold water of the Atlantic ocean $\Theta = 17 \text{ }^\circ\text{C}$ and the warm water of the Mediterranean Sea. The numerical diffusion is also very pronounced in the results obtained using the conventional semi-Lagrangian finite element method. On the other hand, the differences between the results obtained using the fixed and enriched methods in Figure 15 and Figure 16 are very small. For the considered flow and heat conditions, it can be clearly seen that the complicated temperature and flow structures in the Mediterranean Sea being well captured by the proposed multilevel adaptive enriched semi-Lagrangian finite element method. In fact, the computed solutions reveal the physics well in this test example for coupled flow-transport problems. Note that computational results obtained using the proposed method should be compared to observational data of real sea-surface heat transport in the Mediterranean Sea. However, there is no data available until now to carry out this comparison. Thus, at the moment we can only perform simulations and verify that results are plausible and consistent.

6. Conclusions

A multilevel adaptive enriched semi-Lagrangian finite element method has been developed for solving coupled flow-transport problems on unstructured triangular meshes. The proposed method integrates transport part of the equations using the semi-Lagrangian method in the framework of a mixed finite element discretization for the thermal incompressible Navier-Stokes equations in primitive variables. An adaptive L^2 -projection has also been implemented using quadrature rules and to solve the generalized Stokes problem we have used a direct conjugate-gradient solver. This algorithm avoids projection techniques and special corrections for the pressure widely used in the literature for Eulerian-based finite element methods. The main advantage of the new enriched semi-Lagrangian finite element method is that, the convective term that has to be treated carefully in most of Eulerian-based finite element methods has been accurately resolved using the semi-Lagrangian method to interpret the transport nature of the governing equations. Other advantages of the proposed method include (i) the flexibility offered by the finite element discretization to easily handle complex irregular geometries, (ii) the high accuracy inherited from the L^2 -projection in the approximation of solutions at the departure points, (iii) the elimination of projection techniques and special corrections for the pressure in the generalized Stokes problem achieved by using a direct conjugate-gradient solver, and (iv) the improvement in the accuracy and efficiency guaranteed by the multilevel adaptive enrichments increasing the number of quadrature points where it is needed without refining the mesh. As criteria for adaptation of enrichments we have proposed the gradient of the temperature calculated backward at next time level using the semi-Lagrangian approach. Unlike standard h -adaptive finite element methods, the corresponding linear systems in our adaptive enriched semi-Lagrangian finite element method preserve the same structure and size at each refinement in the adaptation procedure. Numerical results were presented for a series of numerical examples including the benchmark problem of flow past a circular cylinder and a heat transport problem in the Mediterranean Sea. For all of these examples, the obtained results have demonstrated the ability of the proposed multilevel adaptive enriched semi-Lagrangian finite element

method to perform very well in the presence of strong gradients and discontinuities without non-physical oscillations and numerical dissipation even when coarse meshes and large time steps are used in the simulations. Results obtained for the problem of heat transport in the Mediterranean Sea have also shown the capabilities of the proposed method to accurately resolve the flow and transport features on coarse meshes and with much fewer degrees of freedom compared to the conventional semi-Lagrangian finite element method. Future work will concentrate on the development of highly accurate error estimates such as a posteriori error estimates to be used as criteria for the multilevel adaptive enrichments.

References

- [1] A. Rips, K. Shoale, R. Mittal, Heat transfer enhancement in laminar flow heat exchangers due to flapping flags, *Physics of Fluids* 32 (6) (2020) 063603.
- [2] M. El Alami, M. Najam, E. Semma, A. Oubarra, F. Penot, Electronic components cooling by natural convection in horizontal channel with slots, *Energy Conversion and Management* 46 (17) (2005) 2762 – 2772.
- [3] L. Khezzar, J. H. Whitelaw, Numerical simulation of fume cupboard performance, *ARCHIVE Proceedings of the Institution of Mechanical Engineers Part C Journal of Mechanical Engineering Science 1989-1996 (vols) 208 (05 1994)*.
- [4] N. S. Lan, S. Viswanathan, Numerical simulation of airflow around a variable volume/constant face velocity fume cupboard, *AIHAJ - American Industrial Hygiene Association* 62 (05 2001).
- [5] Y. Mao, C. Lei, J. Patterson, Unsteady near-shore natural convection induced by surface cooling, *Journal of Fluid Mechanics* 642 (2010) 213–233.
- [6] P. Huang, J. Zhao, X. Feng, Highly efficient and local projection-based stabilized finite element method for natural convection problem, *International Journal of Heat and Mass Transfer* 83 (2015) 357 – 365.
- [7] H. Su, X. Feng, Y. He, Defect-correction finite element method based on crank-nicolson extrapolation scheme for the transient conduction-convection problem with high reynolds number, *International Communications in Heat and Mass Transfer* 81 (2017) 229 – 249.
- [8] H. Su, X. Feng, Y. He, Second order fully discrete defect-correction scheme for nonstationary conduction-convection problem at high reynolds number, *Numerical Methods for Partial Differential Equations* 33 (3) (2017) 681–703.
- [9] J. Wu, P. Huang, X. Feng, A new variational multiscale fem for the steady-state natural convection problem with bubble stabilization, *Numerical Heat Transfer, Part A: Applications* 68 (2015) 777–796.
- [10] M. El-Amrani, M. Seaid, Numerical simulation of natural and mixed convection flows by Galerkin-characteristic method, *Int. J. Numer. Meth. Fluids*. 53 (12) (2007) 1819–1845.
- [11] M. El-Amrani, M. Seaid, A finite element modified method of characteristics for convective heat transport, *Numerical Methods for Partial Differential Equations* 24 (3) (2008) 776–798.
- [12] A. Brooks, T. Hughes, Streamline upwind/Petrov-Galerkin formulations for convection dominated flows with particular emphasis on the incompressible Navier-Stokes equations, *Computer methods in applied mechanics and engineering* 32 (1982) 199–259.
- [13] M. Crochet, V. Legat, The consistent streamline-upwind/Petrov-Galerkin method for viscoelastic flow revisited, *Journal of non-Newtonian fluid mechanics* 42 (1992) 283–299.
- [14] F. Bertrand, L. Demkowicz, J. Gopalakrishnan, N. Heuer, Recent Advances in Least-Squares and Discontinuous Petrov-Galerkin Finite Element Methods, *Computational Methods in Applied Mathematics* 19 (2019) 395–397.
- [15] J. Donea, A Taylor-Galerkin method for convective transport problems, *Int. J. Numer. Meth. Engng.* 20 (1984) 101–119.
- [16] E. Carew, P. Townsend, M. Webster, A Taylor-Petrov-Galerkin algorithm for viscoelastic flow, *Journal of non-Newtonian fluid mechanics* 50 (1993) 253–287.

- [17] X. Cui, S. Chang, G. Li, A two-step Taylor-Galerkin smoothed finite element method for lagrangian dynamic problem, *International Journal of Computational Methods* 12 (2015) 1540004.
- [18] T. J. Hughes, L. P. Franca, G. M. Hulbert, A new finite element formulation for computational fluid dynamics: Viii. The Galerkin/least-squares method for advective-diffusive equations, *Computer methods in applied mechanics and engineering* 73 (1989) 173–189.
- [19] Y. Chai, Z. Gong, W. Li, T. Li, Q. Zhang, Z. Zou, Y. Sun, Application of smoothed finite element method to two-dimensional exterior problems of acoustic radiation, *International journal of computational methods* 15 (2018) 1850029.
- [20] S. Wille, The three-dimensional prolonged adaptive unstructured finite element multigrid method for the Navier-Stokes equations, *Int. J. Numer. Methods. Fluids.* 25 (1997) 371–392.
- [21] M. Wang, T. Sheu, On a compact mixed-order finite element for solving the three-dimensional incompressible Navier-Stokes equations, *Int. J. Numer. Methods. Fluids.* 25 (1997) 513–522.
- [22] C. Liu, Numerical solution of three-dimensional Navier-Stokes equations by a velocity-vorticity method, *Int. J. Numer. Methods. Fluids.* 35 (2001) 533–557.
- [23] D. Lo, K. Murugesan, D. Young, Numerical solution of three-dimensional velocity-vorticity Navier-Stokes equations by finite difference method, *Int. J. Numer. Methods. Fluids.* 47 (2005) 1469–1487.
- [24] S. Deparis, A. Løvgrén, Stabilized reduced basis approximation of incompressible three-dimensional Navier-Stokes equations in parametrized deformed domains, *Journal of Scientific Computing* 50 (2012) 198–212.
- [25] Z. Qian, J. Zhang, Implicit preconditioned high-order compact scheme for the simulation of the three-dimensional incompressible Navier-Stokes equations with pseudo-compressibility method, *Int. J. Numer. Methods. Fluids.* 69 (2012) 1165–1185.
- [26] H. Chen, K. Li, S. Wang, A dimension split method for the incompressible Navier-Stokes equations in three dimensions, *Int. J. Numer. Methods. Fluids.* 73(5) (2013) 409–35.
- [27] C. Subich, K. Lamb, M. Stastna, Simulation of the Navier-Stokes equations in three dimensions with a spectral collocation method, *Int. J. Numer. Methods. Fluids.* 73 (2013) 103–129.
- [28] S. Deparis, M. Deville, F. Menghini, L. Pegolotti, A. Quarteroni, Application of the Rosenbrock methods to the solution of unsteady 3D incompressible Navier-Stokes equations, *Computers & Fluids* 179 (2019) 112–122.
- [29] M. El-Amrani, M. Seaid, A finite element semi-Lagrangian method with L^2 interpolation, *Int. J. Numer. Meth. Engng.* 90 (12) (2012) 1485–1507.
- [30] M. El-Amrani, M. Seaid, An L^2 -projection for the Galerkin-characteristic solution of incompressible flows, *SIAM Journal on Scientific Computing* 33 (6) (2011) 3110–3131.
- [31] M. El-Amrani, M. Seaid, An essentially non-oscillatory semi-Lagrangian method for tidal flow simulations, *Int. J. Numer. Meth. Engng.* 81 (7) (2010) 805–834.
- [32] M. El-Amrani, M. Seaid, Convergence and stability of finite element modified method of characteristics for the incompressible Navier-Stokes equations, *Journal of Numerical Mathematics* 15 (2) (2007) 101–135.
- [33] J. Melenk, I. Babuška, The partition of unity finite element method: Basic theory and applications, *Comput. Methods Appl. Mech. Engrg.* 139 (1996) 289–314.
- [34] A. El-Kacimi, O. Laghrouche, Numerical modelling of elastic wave scattering in frequency domain by the partition of unity finite element method, *Int. J. Numer. Meth. Engng.* 77 (2009) 1646–1669.
- [35] M. Shadi Mohamed, M. Seaid, J. Trevelyan, O. Laghrouche, A partition of unity fem for time-dependent diffusion problems using multiple enrichment functions, *Int. J. Numer. Meth. Engng.* 93 (3) (2013) 245–265.
- [36] S. Sun, J. Liu, A locally conservative finite element method based on piecewise constant enrichment of the continuous Galerkin method, *SIAM Journal on Scientific Computing* 31 (4) (2009) 2528–2548.
- [37] J. Choo, S. Lee, Enriched Galerkin finite elements for coupled poromechanics with local mass conservation, *Computer Methods in Applied Mechanics and Engineering* 341 (2018) 311–332.
- [38] S. Lee, M. Wheeler, Adaptive enriched Galerkin methods for miscible displacement problems with entropy residual stabilization, *Journal of*

Computational Physics 331 (2017) 19–37.

- [39] P. De Sampaio, P. R. M. Lyra, K. Morgan, N. P. Weatherill, Petrov-Galerkin solutions of the incompressible Navier-Stokes equations in primitive variables with adaptive remeshing, *Comput. Methods Appl. Mech. Engrg.* 106 (1-2) (1993) 143–178.
- [40] S. Popinet, Gerris: a tree-based adaptive solver for the incompressible Euler equations in complex geometries, *J. Comp. Physics* 190 (2) (2003) 572–600.
- [41] C. Min, F. Gibou, A second order accurate projection method for the incompressible Navier-Stokes equations on non-graded adaptive grids, *J. Comp. Physics* 219 (2) (2006) 912–929.
- [42] S. K. Patro, R. P. Selvam, H. Bosch, Adaptive h -finite element modeling of wind flow around bridges, *Engineering Structures* 48 (2013) 569–577.
- [43] B. R. Ahrabi, W. K. Anderson, J. C. Newman III, An adjoint-based hp -adaptive stabilized finite-element method with shock capturing for turbulent flows, *Comput. Methods Appl. Mech. Engrg.* 318 (2017) 1030–1065.
- [44] P. De Sampaio, P. R. M. Lyra, K. Morgan, N. P. Weatherill, Petrov-Galerkin solutions of the incompressible Navier-Stokes equations in primitive variables with adaptive remeshing, *Comput. Methods Appl. Mech. Engrg.* 106 (1-2) (1993) 143–178.
- [45] K. Selim, A. Logg, M. G. Larson, An adaptive finite element splitting method for the incompressible Navier-Stokes equations, *Comput. Methods Appl. Mech. Engrg.* 209 (2012) 54–65.
- [46] F. Wang, M. Ling, W. Han, F. Jing, Adaptive discontinuous Galerkin methods for solving an incompressible Stokes flow problem with slip boundary condition of frictional type, *J. Comp. Applied Math.* 371 (2020) 112700.
- [47] P. Roberts, Convection in horizontal layers with internal heat generation: Theory, *J. Fluid Mech.* 30 (1967) 33–49.
- [48] Y. Jaluria, Natural convection heat and mass transfer, Pergamon Press, Oxford, 1980.
- [49] C. Temperton, A. Staniforth, An efficient two-time-level Galerkin-characteristics semi-implicit integration scheme, *Quart. J. Roy. Meteor. Soc.* 113 (1987) 1025–1039.
- [50] A. Allievi, R. Bermejo, A generalized particle search-locate algorithm for arbitrary grids, *J. Comp. Physics* 132 (1992) 157–166.
- [51] D. Dunavant, High degree efficient symmetrical gaussian quadrature rules for the triangle, *Int. J. Numer. Meth. Engng.* 21 (6) (1985) 1129–1148.
- [52] E. Dean, R. Glowinski, On some Finite Elements Methods for the Numerical Simulation of Incompressible Viscous Flow. *Incompressible Computational Fluid Dynamics*, M.D Gunzburger and R.A. Nicolaides eds, Cambridge: Cambridge University Press, 1993.
- [53] M. El-Amrani, M. Seaid, A conjugate gradient algorithm for solving the Galerkin-characteristic approximation of interfacial flows, *Applied Numerical Mathematics* 62 (9) (2012) 1197–1214.
- [54] A. Mueller, Continuously deforming finite element methods for transport problems., PhD dissertation, University of Texas at Austin (1984).
- [55] S. Krishnamachari, L. Hayes, T. Russell, A finite element alternating-direction method combined with a modified method of characteristics for convection-diffusion problems, *SIAM Journal on Numerical Analysis* 26 (6) (1989) 1462–1473.
- [56] A. Horvat, I. Kljenak, M. J., On incompressible buoyancy flow benchmarking, *Numerical Heat Transfer, Part B* 39 (2001) 61–78.
- [57] R. Golani, A. Dhiman, Fluid flow and heat transfer across a circular cylinder in the unsteady flow regime, Vol. 3, 2014, pp. 08–19.
- [58] S. Udhayakumar, T. V. S. Sekhar, R. Sivakumar, Numerical experiments on the study of mixed convection flow in cylindrical geometry, *Numerical Heat Transfer, Part A: Applications* 68 (8) (2015) 870–886.
- [59] D. R. Munday, M. P. Meredith, On the dynamics of flow past a cylinder: Implications for ctd package motions and measurements, *Journal of Geophysical Research: Oceans* 122 (7) (2017) 5708–5728.
- [60] J. Simo, F. Armero, Unconditional stability and long-term behavior of transient algorithms for the incompressible Navier-Stokes and Euler equations, *Comput. Methods Appl. Mech. Engrg.* 111 (1-2) (1994) 111–154.
- [61] M. El-Amrani, M. Seaid, Convergence and stability of finite element modified method of characteristics for the incompressible Navier–Stokes equations, *Journal of Numerical Mathematics* 15 (2) (2007) 101–135.
- [62] X. Song, L. Yu, Air-sea heat flux climatologies in the mediterranean sea: Surface energy balance and its consistency with ocean heat storage, *Journal of Geophysical Research Oceans* (2017) 4068–4087.

- [63] P. T. L. Houpert, S. S. X. Durrieu de Madron, C. E. F. D'Ortenzio, H. Lavigne, Seasonal cycle of the mixed layer, the seasonal thermocline and the upper-ocean heat storage rate in the mediterranean sea derived from observations, *Progress in Oceanography* 132 (2015) 333–352.
- [64] A. Robinson, W. Leslie, A. Theocharis, A. Lascaratos, Mediterranean sea circulation, *Ocean currents* 1 (2001) 19.
- [65] J. Almazán, H. Bryden, T. Kinder, G. Parrilla, *Seminario Sobre la Oceanografía Física del Estrecho de Gibraltar*, SECEG, Madrid, 1988.